AGU PUBLICATIONS

JGR

Journal of Geophysical Research: Space Physics

RESEARCH ARTICLE
10.1002/2016JA023096

Energetic electron precipitation in weak to moderate corotating interaction region-driven storms

Linn-Kristine Glesnes Ødegaard[1], Hilde Nesse Tyssøy[1], Finn Søraas[1], Johan Stadsnes[1], and Marit Irene Sandanger[1]

[1] Birkeland Centre for Space Science, Department of Physics and Technology, University of Bergen, Bergen, Norway

Key Points:
- Use a new and better estimation of loss cone flux to study energetic electron precipitation driven by CIRs
- A linear relationship is found between the energy input into the magnetosphere and precipitation of relativistic electrons
- Precipitation patterns vary in MLT and latitude, attributed to different wave-particle interactions and energy dependent drift periods

Correspondence to:
L.-K. G. Ødegaard,
linnkglesnes@gmail.com

Citation:
Ødegaard, L.-K. G., H. N. Tyssøy, F. Søraas, J. Stadsnes, and M. I. Sandanger (2017), Energetic electron precipitation in weak to moderate corotating interaction region-driven storms, *J. Geophys. Res. Space Physics*, *122*, 2900–2921, doi:10.1002/2016JA023096.

Received 21 JUN 2016
Accepted 14 FEB 2017
Accepted article online 18 FEB 2017
Published online 3 MAR 2017
Corrected 22 MAR 2017

This article was corrected on 22 MAR 2017. See the end of the full text for details.

Abstract High-energy electron precipitation from the radiation belts can penetrate deep into the mesosphere and increase the production rate of NO_x and HO_x, which in turn will reduce ozone in catalytic processes. The mechanisms for acceleration and loss of electrons in the radiation belts are not fully understood, and most of the measurements of the precipitating flux into the atmosphere have been insufficient for estimating the loss cone flux. In the present study the electron flux measured by the NOAA POES Medium Energy Proton and Electron Detectors 0° and 90° detectors is combined together with theory of pitch angle diffusion by wave-particle interaction to quantify the electron flux lost below 120 km altitude. Using this method, 41 weak and moderate geomagnetic storms caused by corotating interaction regions during 2006–2010 are studied. The dependence of the energetic electron precipitation fluxes upon solar wind parameters and geomagnetic indices is investigated. Nine storms give increased precipitation of $> \sim 750$ keV electrons. Nineteen storms increase the precipitation of $> \sim 300$ keV electrons, but not the $> \sim 750$ keV population. Thirteen storms either do not change or deplete the fluxes at those energies. Storms that have an increase in the flux of electrons with energy $> \sim 300$ keV are characterized by an elevated solar wind velocity for a longer period compared to the storms that do not. Storms with increased precipitation of $> \sim 750$ keV flux are distinguished by higher-energy input from the solar wind quantified by the ε parameter and corresponding higher geomagnetic activity.

1. Introduction

Understanding acceleration and loss processes of the energetic electrons in the radiation belts has been a hot topic in recent years (see reviews by *Friedel et al.* [2002], *Millan and Thorne* [2007], *Millan and Baker* [2012], and references therein). The electron energies observed in the radiation belts are much higher than in the solar wind, which means that acceleration takes place inside the magnetosphere. There have been two main theories on how the acceleration to relativistic energies occurs. These are inward radial diffusion (Betatron acceleration) and local wave-particle acceleration [*Friedel et al.*, 2002]. Local wave-particle acceleration, with chorus mode electron cyclotron waves as the most important, has now been commonly accepted as the mechanism responsible for the acceleration to relativistic energies [*Kessel*, 2016]. Studies applying data from the Van Allen Radiation Belt Storm Probes have recently shed light on the question of where in the magnetosphere electrons are accelerated. *Reeves et al.* [2013] investigated a large geomagnetic storm where the Van Allen Probes data show strong evidence of local acceleration at $L \approx 4$ in the equatorial plane.

The electron flux in the outer radiation belt is highly variable and thought to be a result of the competition between acceleration and loss. Geomagnetic storms can both enhance and deplete the energetic electron flux in the radiation belts [*Reeves et al.*, 2003]. Fluxes are commonly seen to be depleted during the main phase of a storm (known as flux "dropout" or the "*Dst* effect"), and in the recovery phase fluxes can recover to prestorm levels, stay depleted or build up to exceed prestorm levels [*Reeves et al.*, 2003; *Meredith et al.*, 2011]. The flux dropout can be a combination of adiabatic and nonadiabatic effects as losses through the magnetopause and atmospheric precipitation [*Millan and Thorne*, 2007]. The drivers of the radiation belt response have not been fully revealed. Many have noted that higher solar wind velocity increases the probability of energetic electron buildup after a storm [e.g, *Kilpua et al.*, 2015], although *Reeves et al.* [2011] pointed out that the relationship is not a linear one.

Storms caused by coronal mass ejections (CMEs) and corotating interaction regions (CIRs) can both produce enhanced radiation belt fluxes. Occurrence rate of CMEs closely follow the solar cycle sunspot number,

while CIRs/high-speed solar wind streams (HSSWS) are more prominent in the declining and minimum phase [*Tsurutani et al.*, 2006a]. *Asikainen and Ruopsa* [2016] found that HSSWSs are more efficient in producing electron precipitation in the declining phase compared to the minimum phase, even though the occurrence of HSSWS is almost equally large in both time periods. CMEs were also, maybe surprisingly, found to be most efficient in producing energetic electron precipitation during the declining phase.

Radiation belt electrons can be scattered in pitch angle by plasma waves and consequently be lost to the atmosphere [e.g., *Tsurutani and Lakhina*, 1997; *Millan and Thorne*, 2007, and references therein]. Plasma waves are generated when there is an instability in the plasma, which redistributes free energy in the system, often associated with, e.g., a density gradient, temperature gradient, magnetic fluctuations, or pitch angle anisotropy in the plasma population. Plasma wave generation is naturally enhanced during disturbed geomagnetic conditions when energy is transferred from the solar wind into the magnetosphere, which strengthen convection of plasma and intensity of currents. During geomagnetic storm time particle precipitation is increased.

Precipitation of radiation belt energetic electrons is of interest to the atmospheric community [e.g., *Andersson et al.*, 2012, 2014a, 2014b; *Rodger et al.*, 2010a; *Rozanov et al.*, 2012; *Sinnhuber et al.*, 2012; *Seppälä et al.*, 2009, 2013; *Seppälä and Clilverd*, 2014; *Seppäla et al.*, 2015; *Turunen et al.*, 2009; *Zawedde et al.*, 2016]. Radiation belt electrons are energetic enough to penetrate deep into the mesosphere where their energy deposition increases the production rate of NO_x and HO_x, which in turn will reduce the ozone density in catalytic processes [*Sinnhuber et al.*, 2012]. During polar winter the precipitation effects can be long lived and potentially influence temperature and winds, causing dynamical signatures that can propagate all the way down to the surface [*Seppälä et al.*, 2009; *Sinnhuber et al.*, 2012]. Quantifying the energetic electron precipitation (EEP) fluxes and the subsequent atmospheric effects still remains an unsolved, important question. *Anderson et al.* [2015] show that small geomagnetic storms affect the radiation belt acceleration and loss in much the same way as large storms, comparing their results with the larger storms studied by *Reeves et al.* [2003]. Several studies indicate that also small and frequently occurring storms associated with HSSWS significantly impact NO_x and HO_x production rates in the mesosphere [*Andersson et al.*, 2012; *Daae et al.*, 2012; *Andersson et al.*, 2014a, 2014b; *Zawedde et al.*, 2016].

EEP in relation to geomagnetic storms has been the focus of many recent studies [e.g., *Asikainen and Ruopsa*, 2016; *Blum et al.*, 2015; *Clilverd et al.*, 2010; *Kavanagh et al.*, 2012; *Meredith et al.*, 2011; *Rodger et al.*, 2010a, 2010b, 2015]. However, all studies have different approaches to quantifying the precipitated electron flux. An electron is precipitated when it is lost to the atmosphere by collisions with atmospheric particles. This process takes place over a range of altitudes as the atmosphere gets denser, but it is custom to use 100–120 km as a boundary below which most particles are considered to give up their energy.

Currently, the best alternative for measuring particles in the atmospheric loss cone is the National Oceanic and Atmospheric Administration (NOAA) Polar Orbiting Environmental Satellites (POES), covering a large range of magnetic local times (MLT) at 800–850 km. The almost identical Medium Energy Proton and Electron Detectors (MEPED) flown on POES constitutes probably the longest running continuous measurements of energetic electrons and protons to date, with a wide range of energies sampled. The two electron telescopes flown on each satellite see only a limited range of pitch angles as they go along the satellite track [*Evans and Greer*, 2000]. At high latitudes, the 0° detector, which points radially outward, will measure mostly particles near the center of the atmospheric loss cone, while the 90° detector (mounted approximately 90° away from the first detector) measures a mix of trapped and precipitating particles [*Rodger et al.*, 2010a, 2010c; *Nesse Tyssøy et al.*, 2016]. Studies utilizing only one of the telescopes [e.g., *Meredith et al.*, 2011] will underestimate (0°) or overestimate (90°) the total precipitated flux in any given location. *Rodger et al.* [2013] and *Asikainen and Ruopsa* [2016] used the geometric mean between the count rates of the two telescopes. *Rodger et al.* [2013] found that the geometric mean of > 30 keV electron fluxes was in agreement with riometer absorption observations when the flux was $> 10^6$ ($cm^{-2}\ s^{-1}\ sr^{-1}$), but that the geometric mean fluxes underestimated absorption when fluxes were $< 10^6$. Using only riometer observations gives no energy resolution, only the integral flux of electrons with energy $E > 30$ keV assuming a specific spectral form [e.g., *Kavanagh et al.*, 2012]. Other satellites in low polar orbit (e.g., Solar Anomalous and Magnetospheric Particle Explorer, or SAMPEX) have a poor coverage of the loss cone [*Blum et al.*, 2015].

In the present study we utilize a physics-based technique which quantifies the electron flux lost below 120 km altitude from the two NOAA POES MEPED detectors [*Nesse Tyssøy et al.*, 2016]. The method estimates the

atmospheric loss cone size for all locations on Earth (above ±40° latitude) and combines the measurements from MEPED 0° and 90° detectors together with theoretical pitch angle distributions from wave-particle interactions [*Kennel and Petschek*, 1966; *Theodoridis and Paolini*, 1967] to determine the total precipitated flux at 120 km. This offers a new and optimized method to study radiation belt losses to the atmosphere, especially in geomagnetic disturbances caused by HSSWS/CIRs, which are known to have a weak geomagnetic signature [*Tsurutani et al.*, 2006a], and often weaker diffusion. In these cases, the MEPED 0° detector may register only a few counts near the center of the loss cone, whereas there may still be significant fluxes if the whole bounce loss cone is considered.

We identify 41 isolated events and perform a superposed epoch analysis. The events are sorted into groups according to their increase or decrease in precipitating fluxes with energy larger than approximately 300 keV and 750 keV poststorm compared to prestorm. We examine their relationship to geomagnetic indices and solar wind parameters. Last, we investigate one of the features that appears to stand out in the group of enhanced high-energy fluxes, namely the flux dependence on the energy input to the magnetosphere from the solar wind, quantified using the *Akasofu* [1981] epsilon parameter (ϵ) (given in SI units by *Koskinen* [2002]). The goal is to be able to determine which storms are likely to cause increased precipitation of high-energy electrons and to single out the potential parameters to be used in a future parametrization of EEP.

2. Data and Methods

The MEPED electron detectors suffer from contamination from protons [*Evans and Greer*, 2000; *Yando et al.*, 2011; *Green*, 2013]. In addition, the geometric factor for the detectors varies with energy [*Yando et al.*, 2011; *Green*, 2013]. The nominal energy boundary of the lowest electron channel (E1) is 30 keV. *Yando et al.* [2011] found that the geometric factor for 30 keV was 2×10^{-3} cm^2 sr, only 20% of the 1×10^{-2} cm^2 sr given in the Instrument Description [*Evans and Greer*, 2000; *Green*, 2013]. *Green* [2013] used a wide range of input spectrum shapes to deduce the appropriate geometric factor, energy value, and flux conversion that works best regardless of the spectrum. However, the energy values they provided were different if a power law spectrum or an exponential spectrum was used. We have done an analysis which is somewhat similar to *Green* [2013], giving a more consistent result independent of the spectrum shape. The method is outlined in Appendix A. The new geometric factors are given in Table A1, together with the new, optimized lower energy threshold for each of the electron channels.

The proton measurements from MEPED are corrected for degradation using results obtained by *Sandanger et al.* [2015], *Ødegaard et al.* [2016], and *Ødegaard* [2016], before being used to remove the proton contamination from the electron measurements. The contaminating proton energies for E1, E2, and E3 are $>$ 210 keV, $>$ 280 keV, and $>$ 440 keV, respectively [*Evans and Greer*, 2000; *Yando et al.*, 2011]. From the corrected and interpolated proton spectrum, the flux of protons at these energies can be retrieved and subsequently subtracted from the electron flux.

The method of using the proton telescope to estimate the contaminating fluxes in the electron telescope is an approximation, since there will be statistical differences of the actual proton flux in the two telescopes. However, in most of our storms the proton flux is orders of magnitude smaller than the electron flux. When the estimated contaminating flux is larger than 50% of the total (uncorrected) flux measured in the electron detector, we discard the data. On average, 2–3% of the data is removed in each channel from the 90° detector and 4–7% from the 0° detector in each storm. Most of the data removed are between 60 and 70° geomagnetic latitude, and more data are removed in the dusk sector than the rest of the hemisphere. There is generally more proton contamination in E1 and E2 than in E3, especially in the 0° detector. Care should always be taken when using the MEPED electron data, especially during periods of high proton fluxes (e.g., during CMEs).

Due to the response of relativistic electrons in the highest proton channel (P6) of the MEPED instrument, we are able to construct a fourth electron channel measuring higher-energy electrons, as described in *Nesse Tyssøy et al.* [2016]. Together with the P6 electron measurements, we have an integral spectrum of electron fluxes at energies $>$ 43 keV, $>$ 114 keV, $>$ 292 keV, and $>$ 756 keV (see Table A1). For simplicity, we refer to the MEPED channels as E1, E2, E3, and P6, which is common when using the MEPED data. In this work, we study the fluxes in each energy channel separately.

Lastly, we use the technique described in *Nesse Tyssøy et al.* [2016] to construct the local atmospheric Bounce Loss Cone (BLC) fluxes from the electron fluxes measured by the 0° and 90° detectors, in all four energy

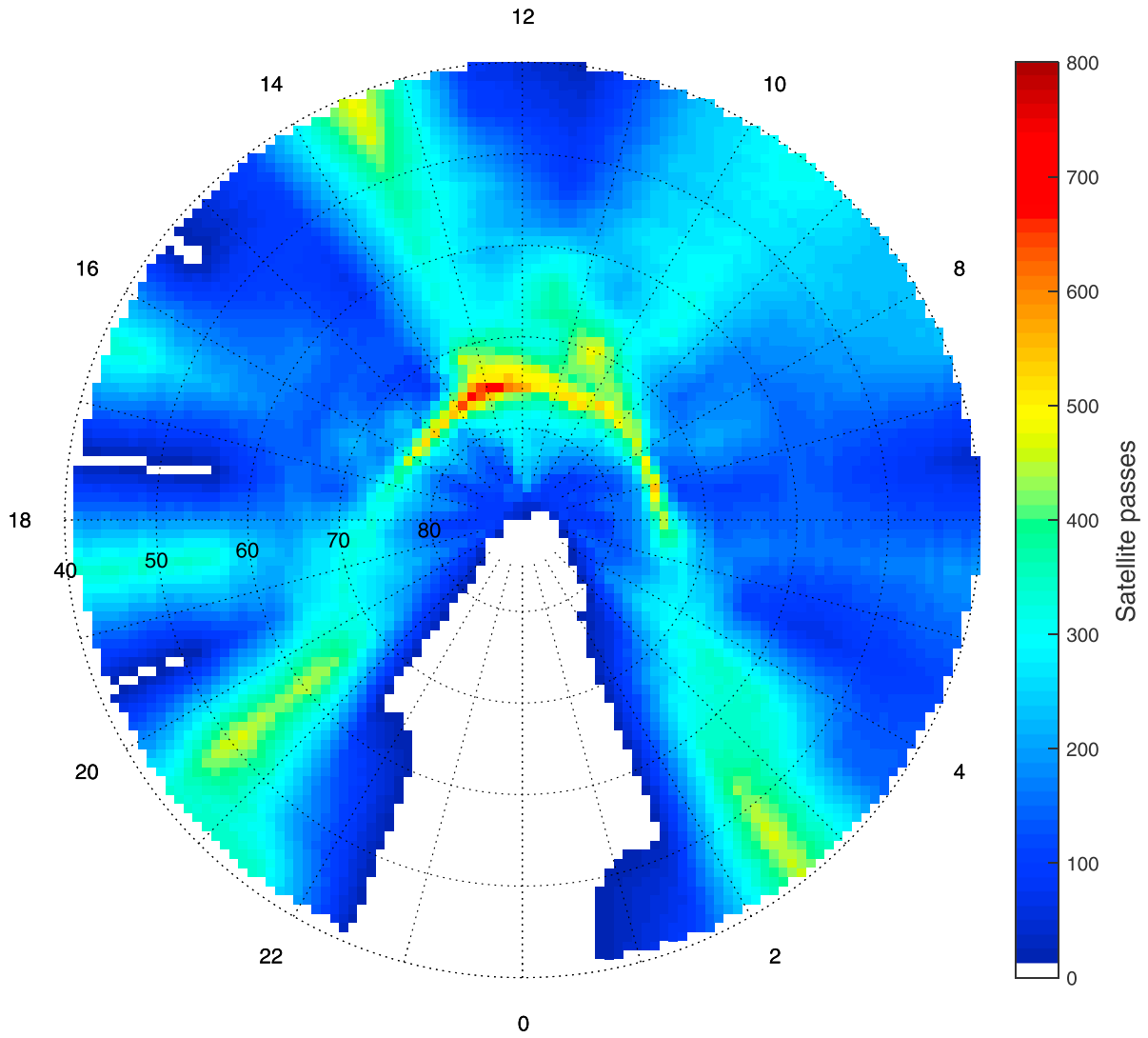

Figure 1. The total number of times a satellite entered a box of size 1 h MLT and 1° corrected geomagnetic latitude during 41 storms.

channels. For full details concerning the method of obtaining BLC fluxes, we refer the reader to *Nesse Tyssøy et al.* [2016]. When the 0° detector is measuring fluxes close to the noise level of the instrument, the uncertainty in the estimated BLC fluxes will increase. *Nesse Tyssøy et al.* [2016] therefore caution against using the estimated BLC fluxes during very quiet times. In this study we have not applied any filter on low fluxes but keep in mind this advice when we interpret our findings.

We use all available POES satellites throughout a storm and data from the Northern Hemisphere. The data are binned in 1 h MLT versus 1° corrected geomagnetic (CGM) latitude boxes and averaged in 2 h intervals. The hemispheric coverage varies from storm to storm, depending on year and how many NOAA POES satellites are in operation at the time. None of the satellites' orbits cross near 24 MLT in the Northern Hemisphere, which results in limited coverage between 22 MLT and 2 MLT. The remaining MLTs are well represented, as shown in Figure 1. For the epoch analyses we split the hemisphere into four MLT sectors and study the time evolution of the average flux in each sector. These are 2–6, 6–12, 12–18, and 18–22 MLT.

The field of view of the 90° telescope relative to the BLC varies over the satellite orbit. At 55°–68° invariant latitude the 90° telescope will mainly measure not only trapped particles but also particles inside the Drift Loss Cone. Most of the time the trapped population is orders of magnitude higher than the precipitated one [*Rodger et al.*, 2010c]. For a given L shell in this region, when averaged over all geographic longitudes, the stably trapped particle fluxes will tend to dominate the average fluxes. We henceforth consider these average fluxes (measured by the 90° telescope) as the trapped fluxes. With this precaution, we will therefore use, similar to, e.g., *Horne et al.* [2009] and *Meredith et al.* [2011], the 90° flux as a qualitative proxy for how the trapped fluxes in the radiation belts behave and contrast these with the precipitating BLC fluxes.

We focus on geomagnetic disturbances created by HSSWS and typical CIR signatures which originate from solar coronal holes. A CIR can be identified in the solar wind velocity as a change from a slow speed (approximately 300–400 km/s) to a high speed (approximately 600–800 km/s) over the course of 1–2 days. Ahead of the solar wind velocity increase there is a region with compressed magnetic field, where the corotating high-speed solar wind interacts with the preceding slow solar wind [*Richardson*, 2006]. The compression

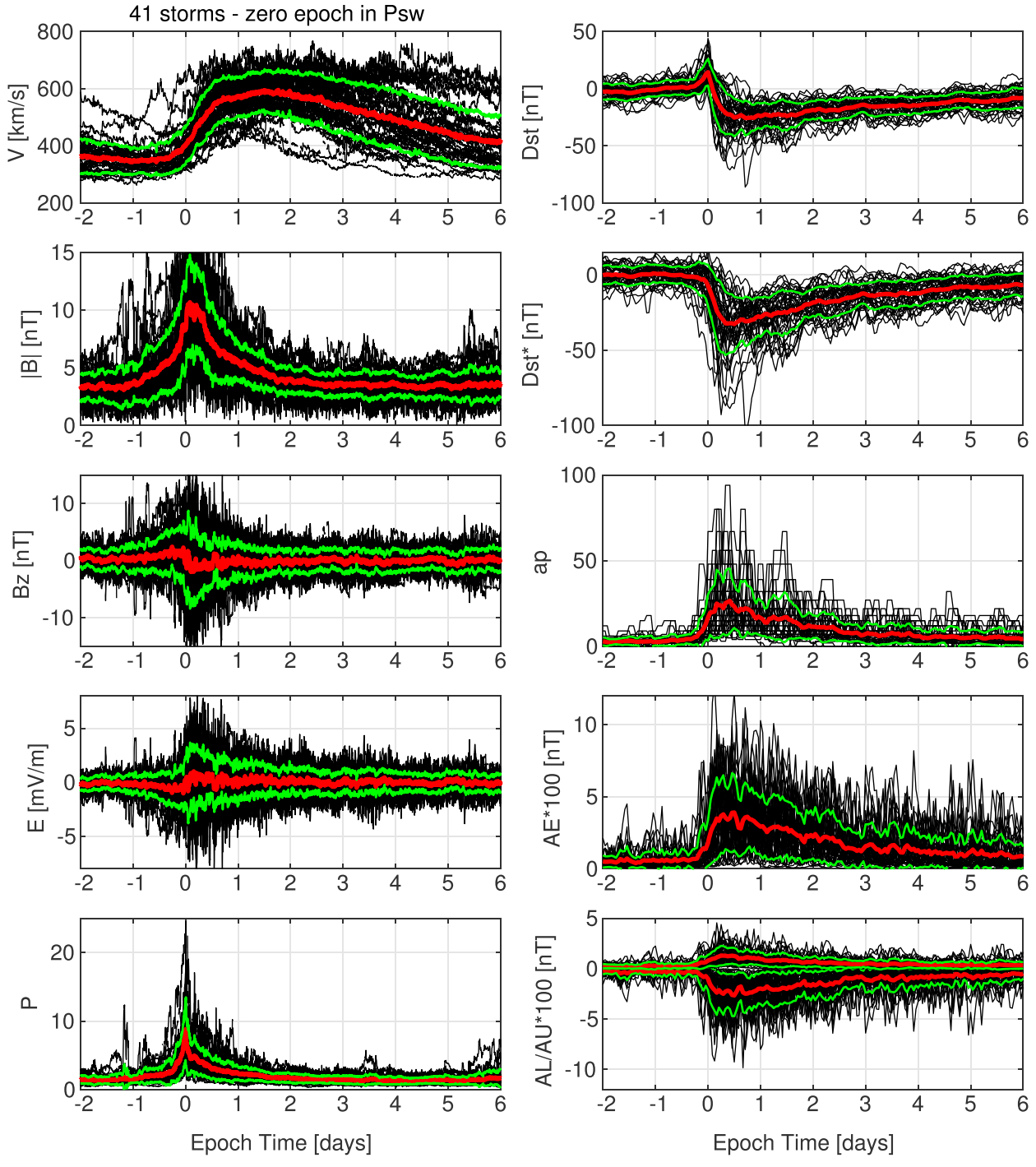

Figure 2. Superposed epoch analysis of 41 CIR/HSSWS storms from 2006 to 2010. (left column) Five-minute OMNI data are plotted for the solar wind measurements. (right column) One-hour resolution geomagnetic indices are plotted (3 h for *ap*). The mean is plotted in thick red lines, with the standard deviation of the data given as green lines. The timing of zero is described in the text in section 2 and listed in Table B1.

is also seen in the solar wind plasma density and pressure [*Tsurutani et al.*, 2006b]. Due to the pressure enhancement, CIR storms will often display a positive gradient in the *Dst* index before the start of the storm, although not as abrupt as the CME storm sudden commencement [*Borovsky and Denton*, 2006; *Tsurutani et al.*, 2006b].

To ensure that an identified CIR was geoeffective, we visually inspected the 1-hourly *Dst* index for typical storm signatures and checked it against a published online catalogue of coronal holes (http://www.solen.info/solar/coronal_holes.html). No criterion was put on the size of the storms with respect to the *Dst* index, but the conditions 2 days prior to the main phase of the event should be quiet (average $Dst > -20$ nT). We focus on the years 2006–2010 which are in the declining and minimum phase of the solar cycle, where CIRs dominate the geomagnetic activity. When we excluded the few periods of coronal mass ejections [*Richardson and Cane*, 2010], we were left with a selection of 41 weak to moderate events, listed in Table B1. Many would not be classified as geomagnetic storms by usual criteria [e.g., *Gonzalez et al.*, 1994]; 12 events have -20 nT $\geq$ minimum $Dst > -30$ nT, 21 events have -30 nT $\geq$ minimum $Dst \geq -50$ nT, and 8 have minimum $Dst < -50$ nT.

We use the solar wind pressure pulse arrival at the bow shock nose (from the OMNI database) as the zero epoch in our analyses, characterized by the maximum pressure. We use solar wind data with a 5 min cadence. When the solar wind pressure data are ambiguous, we select the time when the main phase of the storm starts

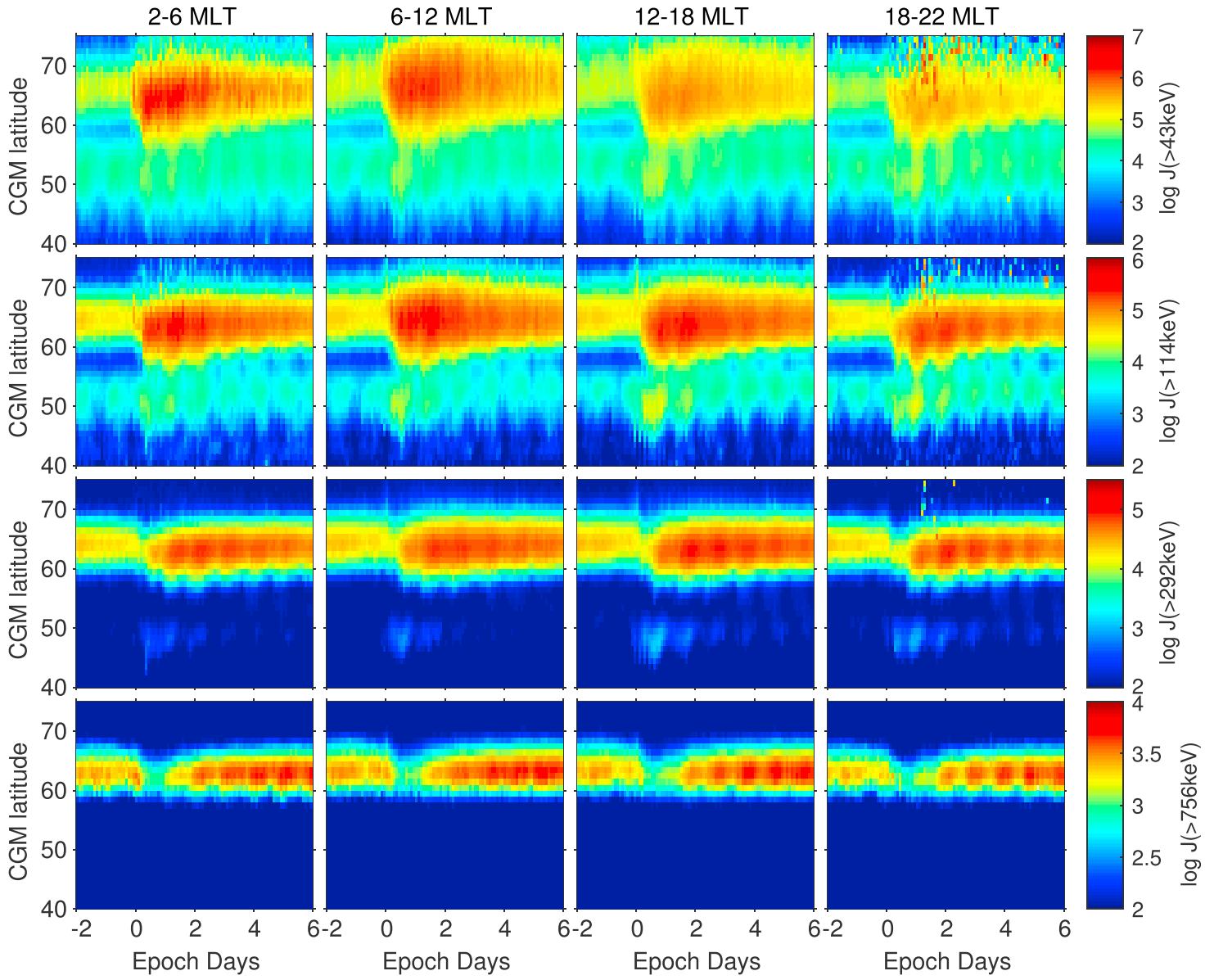

Figure 3. Superposed epoch analysis of 41 CIR/HSSWS storms from 2006 to 2010, measurements from the 90° detector of the MEPED instrument. All available NOAA POES satellites were used, and the data were binned in a 1° CGM latitude versus 2 h grid. The fluxes are plotted in logarithmic color scale (in units of integral flux [cm^{-2} s^{-1} sr^{-1}]) and the data are divided into the four sectors (from left to right) 0–6 MLT, 6–12 MLT, 12–18 MLT, and 18–24 MLT. (top to bottom) E1, E2, E3, and P6 flux are shown. Note that the range of the colorbar is different for the four channels.

in the *Dst* index. This is found by identifying the timing of the maximum value in the *Dst* index preceding the *Dst* minimum reached at the peak of the storm.

For the total epoch length we use 2 days prior to zero epoch and 6 days after the zero epoch, 8 days in total. The exact timing used for zero epoch in each storm is listed in Table B1.

3. Superposed Epoch Analysis

The solar wind data for all 41 events are plotted in Figure 2 with a 5 min resolution and the geomagnetic indices with an hourly resolution (except for *ap*, which has a 3 h resolution). The mean of all events is plotted in red with the standard deviation of the data given in green. Individual storms are plotted in black. The pressure corrected *Dst* index, *Dst**, is calculated as

$$Dst^* = Dst - (15.8 * P^{0.5}) + 20 \quad (1)$$

where P is the solar wind pressure with a 1 h resolution [*Burton et al.*, 1975].

The average event is small with a minimum *Dst* of −25 nT in the main phase, which is reached about 12 h after zero epoch. The average prestorm conditions are quiet with northward interplanetary magnetic field (IMF $B_Z > 0$) and slow solar wind velocity $V_{SW} \sim 350$ km/s. The solar wind velocity starts to increase about 6 h before zero epoch and reaches a plateau of maximum ~ 600 km/s at 18–48 h. The IMF B_Z turns southward right before zero epoch and is predominantly southward for approximately 12 h. IMF B_Z oscillates rapidly, seen as a widening of the envelope of B_Z in Figure 2. There is an increase in the IMF |B| from about −1 day to about 2 days after zero, which is typical for CIR storms. The *AL* index is stronger than the *AU* index, also a typical feature of CIR or HSSWS storms [*Tsurutani et al.*, 2006a]. The mean *Dst* and *Dst** indices do not recover fully in

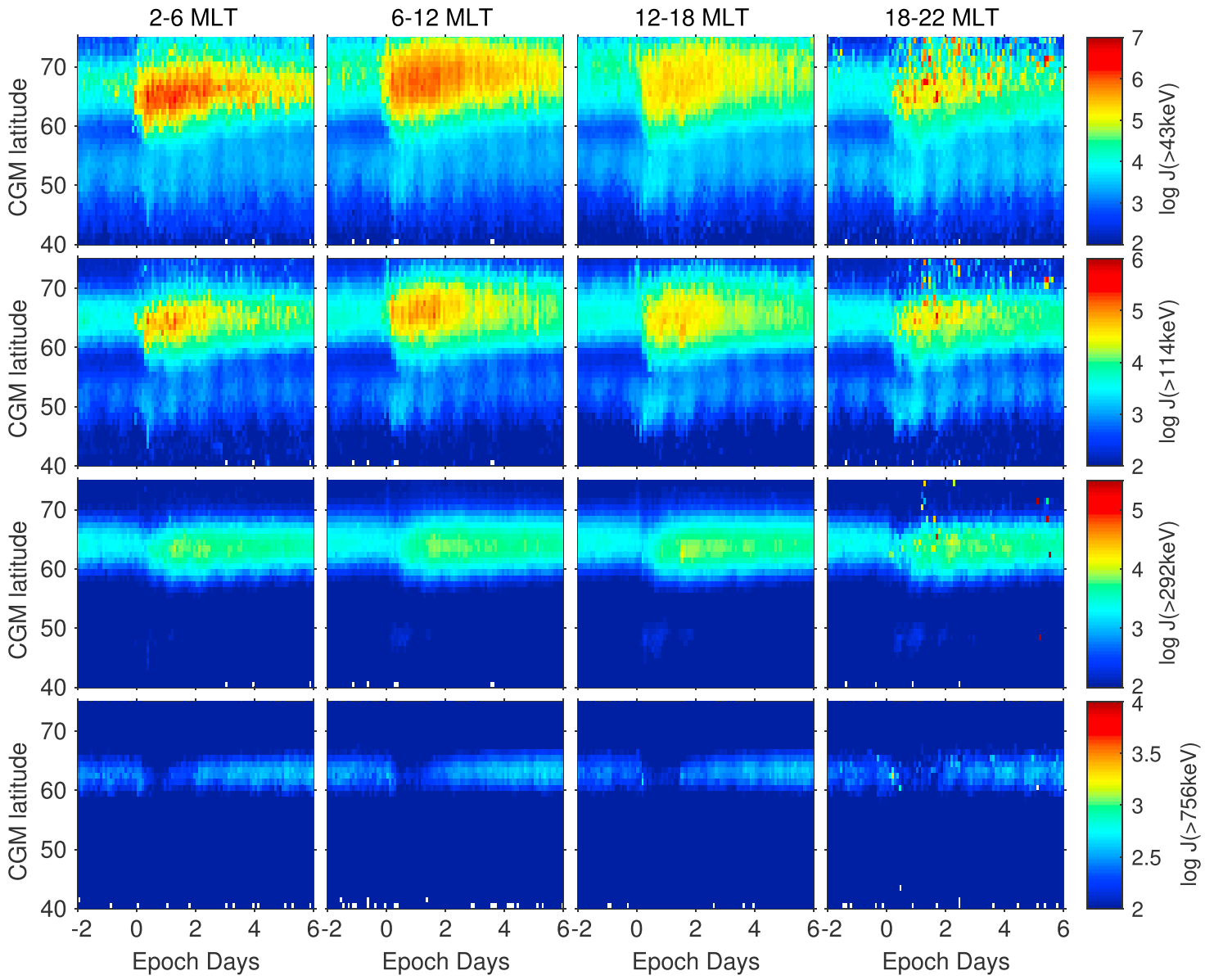

Figure 4. Same as Figure 3 but for the BLC fluxes. The color scale is logarithmic in units of integral flux (cm^{-2} s^{-1} sr^{-1}).

the 6 days after zero epoch. Recovery phases for CIR storms can last from days to many weeks [*Tsurutani et al.*, 2006a]. This is because new particles are injected in the ring current and also in the recovery phase of such storms [*Søraas et al.*, 2004].

Figure 3 shows the mean behavior of the trapped radiation belt fluxes in the 41 events as a function of time and geomagnetic latitude. The four MLT sectors are plotted from left to right, and the four energy channels from top to bottom in ascending order. The color scale is logarithmic and different for each energy channel. The standard deviation of the mean is found to be around 1 order of magnitude smaller than the mean (not shown). The specific value of the standard deviation varies with latitude and is generally largest at the latitudinal boundaries of the region of enhanced flux and smallest at latitudes near the maximum flux (CGM latitude ~60°–70°). The standard deviation of the mean is also higher in the 18–22 MLT sector high-latitude region, due to the poorer satellite coverage as well as a smaller data set due to proton contamination.

We see both the inner (~45°–55° CGM) and outer radiation belt (~60°–75°) in the two lowest energy channels. The inner belt is present also before the storm. There is a hint of electrons in the E3 channel during the main phase of the storm in the inner belt, but generally the high-energy electrons are concentrated in the outer belt.

The E1 trapped fluxes are enhanced abruptly around zero epoch, first seen at CGM latitudes near 65° in the 2–6 and 18–22 MLT sectors, and somewhat higher latitudes in the 6–12 and 12–18 MLT sectors. In the 12–18 and 18–22 MLT sectors, the maximum flux is lower compared to the 2–6 and 6–12 MLT sectors. Most probably, this feature is created by the direction of electron drift path around the Earth, causing some of the particles to be lost before they can complete the full drift path. *Lam et al.* [2010] show that precipitation measured in the E1 channel of the electron MEPED detector is correlated with chorus waves, causing a higher loss of particles between 22 and 12 MLT compared to between 12 and 22 MLT. *Summers et al.* [2007] give a detailed overview of how each wave mode (chorus, hiss, and electromagnetic ion cyclotron (EMIC)) contribute to the total electron loss rate depending on MLT, energy, and L shell of the electron.

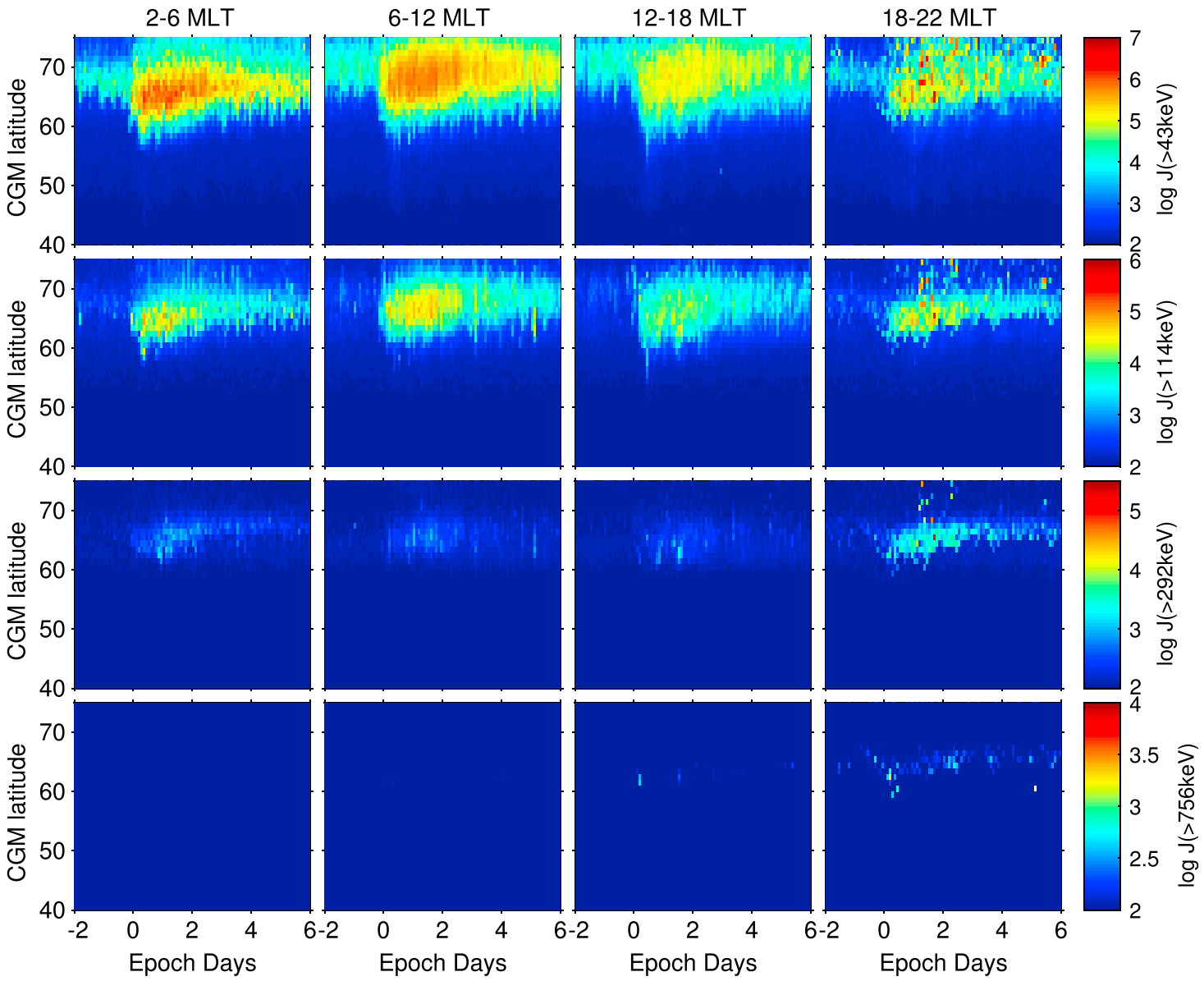

Figure 5. Same as Figure 3 but for the 0° detector. The color scale is logarithmic in units of integral flux (cm^{-2} s^{-1} sr^{-1}).

In the 6–12 and 12–18 MLT sectors, the enhancement is seen in a broader CGM latitude band compared to the two other sectors. The flux cutoff is also seen at higher latitudes in the 6–12 and 12–18 MLT sectors compared to the 18–22 and 2–6 MLT sectors, a feature of the radiation belts that was early shown to exist [*Frank et al.*, 1964; *Williams and Palmer*, 1965]. There is clearly a difference between the sectors in both onset latitude, the maximum flux, and how broad the latitude range of precipitation is. The irregular fluxes seen at high latitudes in the E1 and to some degree the E2 channels in the 18–22 MLT sector is, as already mentioned, caused by a combination of limited satellite coverage at these latitudes (see Figure 1) and the larger proton contamination in this sector compared to the rest of the sectors. The amount of data removed due to contamination in this sector is higher than in the other sectors for all of the storms. This means that the remaining data set is smaller than in the other three sectors, and thus, the electron flux in the 18–22 MLT sector is connected with a larger uncertainty.

The enhancement of E2 flux is delayed by a few hours compared to the E1 flux, both at onset and maximum. In E2, the magnitude of the maximum flux is more similar in all MLT sectors than in E1, consistent with a faster drift of higher-energy electrons. We still see that the dayside fluxes cover a wider range in CGM latitude than the nightside fluxes. The E3 and P6 fluxes are even more delayed with respect to the E1 fluxes and display a clear flux dropout for some time after zero epoch. There is also a daily modulation of the fluxes (most easily seen in the P6 channel) which may be due to variations in the magnetic field with geographic longitude (and thus with UT time, when sampled at a constant MLT sector) and also loss of particles in the Southern Hemisphere.

The BLC fluxes are plotted in Figure 4 in the same manner as the trapped fluxes, and the color scale of each channel is the same in the two figures for easier comparison. Also, for this data, the standard deviation of the mean is found to be around an order of magnitude smaller than the mean (not shown). The largest precipitation occurs in the outer belt, but there also appears to be precipitation from the inner belt in the two lower energy channels which would be completely missed if only the 0° detector was used, as shown in Figure 5. This should, however, be interpreted with some caution as the 0° fluxes are close to the detector background of

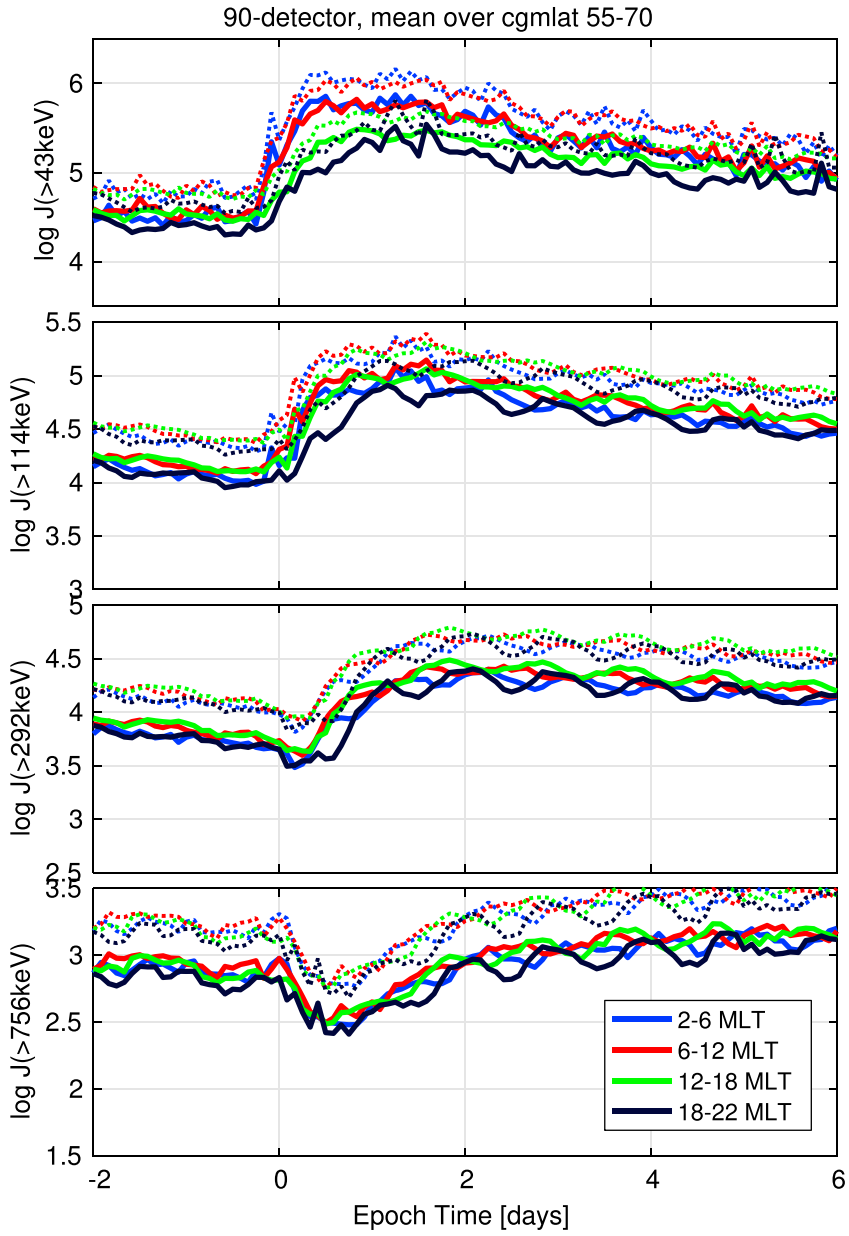

Figure 6. Superposed epoch analysis of 41 CIR/HSSWS storms from 2006 to 2010, measurements from the 90° detector of the MEPED instrument. All available NOAA POES satellites were used, and for each of the sectors 0–6 MLT, 6–12 MLT, 12–18 MLT, and 18–24 MLT the flux was averaged between CGM latitudes 55 and 70°. (top to bottom) E1, E2, E3, and P6 flux are shown. Note that the range on the *y* scale is different for the four channels, and logarithmic is in units of integral flux (cm^{-2} s^{-1} sr^{-1}). The sum of mean flux and the positive standard deviation of the mean flux for each storm is plotted as dotted line.

the MEPED instrument. *Nesse Tyssøy et al.* [2016] pointed out that the BLC fluxes might be associated with large errors in these cases. We note that the E1 and E2 BLC fluxes are higher in the 2–6 and 6–12 MLT sectors, consistent with a higher loss in this region due to chorus waves [*Lam et al.*, 2010]. This fits with our interpretation of the E1 and E2 trapped fluxes in Figure 3.

To determine how much the trapped and precipitated fluxes increase, we take the average flux over 55°–70° CGM latitude and compare the maximum flux after zero epoch to the mean flux 48 to 36 h before zero epoch. The time series of the mean fluxes are plotted in Figures 6 and 7 for the trapped and BLC fluxes, respectively. The trapped flux (BLC flux) in the E1 channel increases by a factor of 9–18 (17–44), depending on sector. The maximum flux in the dayside sectors is higher than the nightside sector, and the maximum is reached approximately 0.5 days earlier. The smallest increase is found in the 12–18 MLT and 18–22 MLT sectors in both the trapped and BLC fluxes. In the E2 channels, the trapped flux (BLC flux) increases by a factor of 8–11 (9–15), with the highest increase in the 6–12 MLT sector. The 18–22 MLT maximum is the smallest of the four sectors and also delayed with respect to the other sectors. The MLT dependence of the increase is less prominent in the E3 and P6 channels, where the trapped flux (BLC flux) increases by factors of ~6 (~3) and ~3 (~1.5) in the two channels, respectively.

There is a seemingly interesting feature in the E3 and P6 channels in the 18–22 MLT sector. The average BLC fluxes increase near zero epoch when the average of the trapped fluxes is decreasing. This may be evidence of a process of strong pitch angle scattering, since a simultaneous flux increase in the 18–22 MLT sector is found in the 0° fluxes, shown in Figure 5. However, closer inspection of the behavior of each single storm reveals that

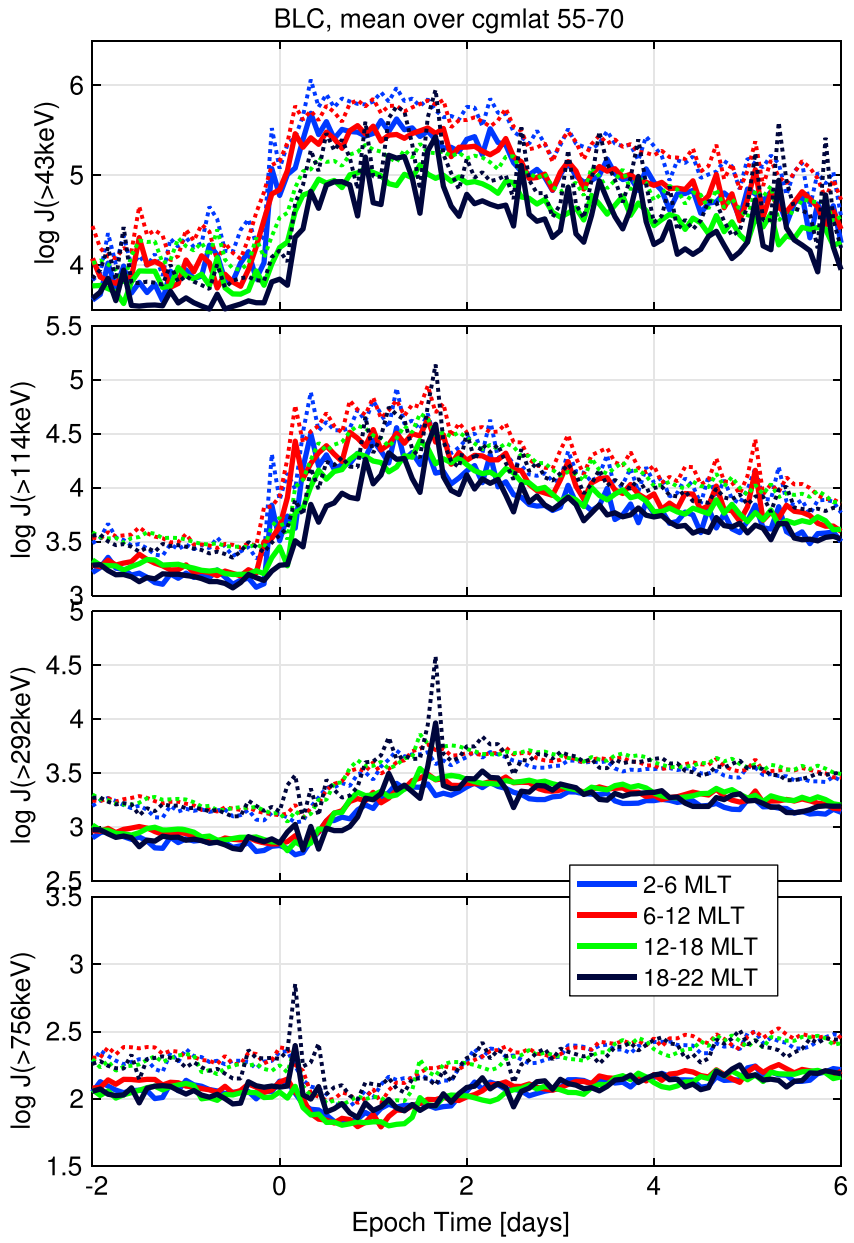

Figure 7. Same as Figure 6 but for the BLC fluxes. Note that the range on the *y* scale is different for the four channels, and logarithmic is in units of integral flux (cm^{-2} s^{-1} sr^{-1}).

the enhancement is not a general feature for all storms but caused by a few storms with high precipitation of high-energy electrons in the early recovery phase. The P6 channel is only used for electron measurements when the flux of high-energy protons in P4 and P5 of the MEPED proton detector is significantly lower than the flux in the P6 channel, and this feature is therefore not caused by protons.

The timing of the precipitation, the MLT dependence, and the limited latitude distribution (which can be seen in Figure 4) are consistent with pitch angle scattering by EMIC waves. EMIC waves usually occur at the duskside in the storm main phase as they are generated by ring current injections. Their confinement in latitude is related to the location of the plasmapause, which is close to $L = 4$ and acts as a wave guiding boundary for the EMIC waves. Around $L = 4$ the hot ring current particles overlap with the cold plasmasphere and allow generation and propagation of EMIC waves.

4. Sorting Events by Increase/Decrease in High-Energy BLC Flux

Still an unsolved question is what separates storms that enhance the flux of relativistic electrons in the magnetosphere and the storms that do not. From the perspective of the atmospheric modeling community, we are interested in knowing whether a storm will produce enhanced *precipitation* of relativistic electrons, which penetrate deep into the atmosphere. We therefore divide our events into groups according to whether the poststorm BLC fluxes of P6 and E3 are greater than the prestorm fluxes. We compare the mean BLC flux of the 2 days before zero epoch to the mean of days 4 and 5 after zero. The average BLC flux over all MLT sectors between CGM latitudes 55° – 70° is compared in the two time intervals. The events are divided into three groups: (1) post-P6 flux > 2× pre-P6 flux; (2) post-E3 flux > 2× pre-E3 flux and post-P6 flux ≤ 2×pre-P6 flux; and (3) post-E3 flux ≤ 2× pre-E3 flux and post-P6 flux ≤ 2×pre-P6 flux, where flux here is the BLC flux specifically. We refer to the groups as 1, 2, and 3, respectively.

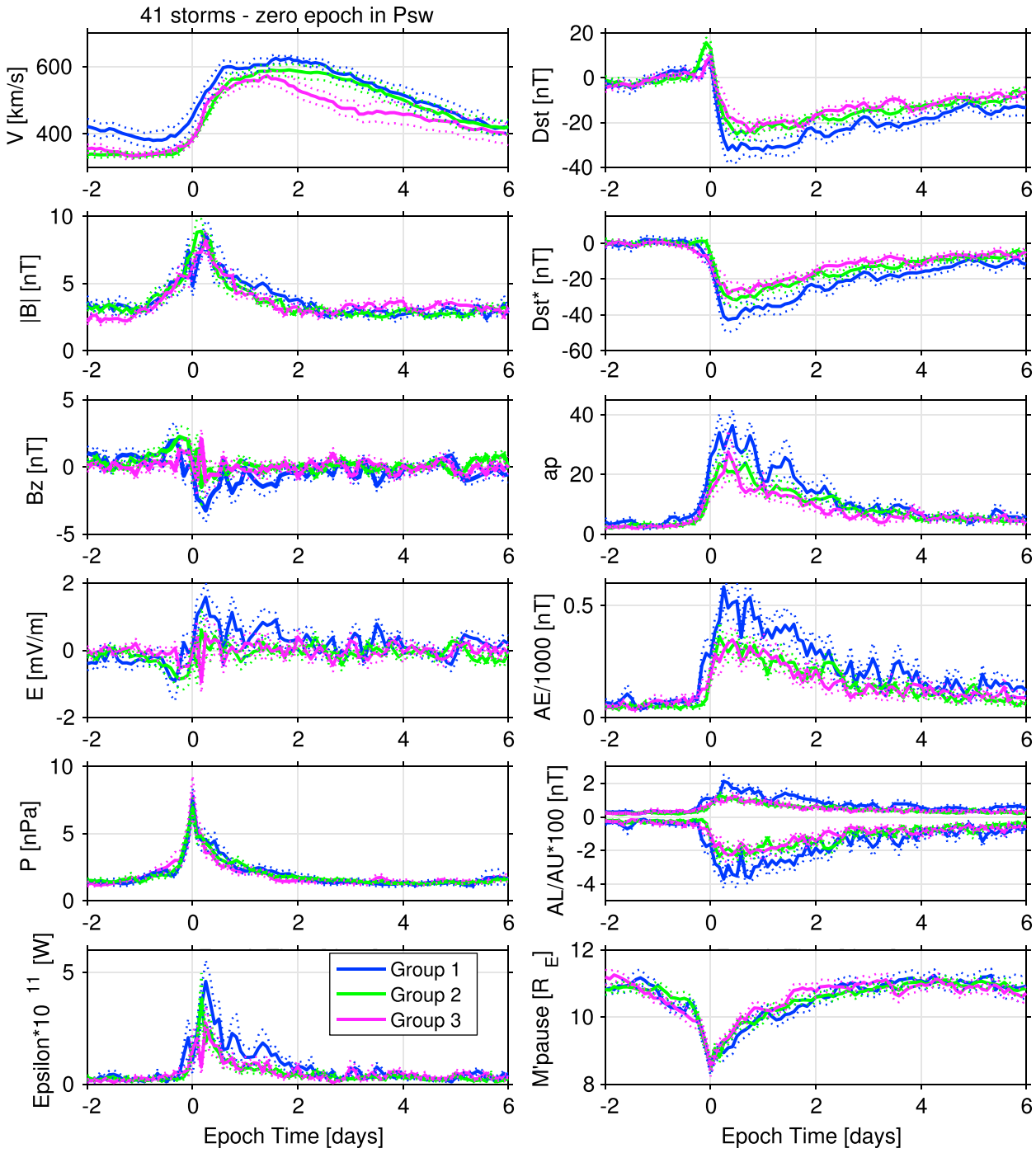

Figure 8. Superposed epoch analysis of 41 CIR/HSSWS storms from 2006 to 2010. Here we have averaged all the data in Figure 2 with a 2 h epoch resolution as was used on the flux data. We have divided all the storms into three groups (see text for description). The mean ± the standard deviation of the mean of each group is plotted as dotted lines.

The criteria of postflux being more than twice the preflux level are in line with previous studies of radiation belt enhancement or depletion [*Reeves et al.*, 2003; *Anderson et al.*, 2015]. Applying the criteria, 9 of 41 events (22%) belong in group 1. Of the remaining 32 events, 19 belong in group 2 (46%), whereas the last 13 events belong in group 3 (32%). Of the group 3 events, 10 decrease in P6 flux, while the remaining 3 have a ratio between 1 and 2.

Figure 8 shows the superposed epoch analysis of the solar wind parameters and geomagnetic indices for the different groups. The mean of group 1 is plotted in blue, group 2 in green, and group 3 in magenta. The sum of mean and its respective standard deviation of each group is plotted in dotted line with the same color as the mean. The maximum solar wind pressure is similar in all three groups ($P_{SW} \sim 7.5$), although group 3 has the largest maximum. Group 1 is separated by having the largest positive solar wind electric field, sustained higher than groups 2 and 3 for approximately 2 days following zero epoch. This indicates a larger energy input to the magnetosphere from the solar wind and also causes these storms to have a larger geomagnetic signature, seen in all the indices. Solar wind electric field is calculated as

$$E = -V \times B_Z \tag{2}$$

and we see that it is mainly the B_Z component that separates groups 1 and 2 from each other, since the solar wind velocity measurements for these two groups are very similar. Even though the solar wind velocities of groups 1 and 2 are very similar, group 2 starts from a lower mean speed, more similar to group 3 events

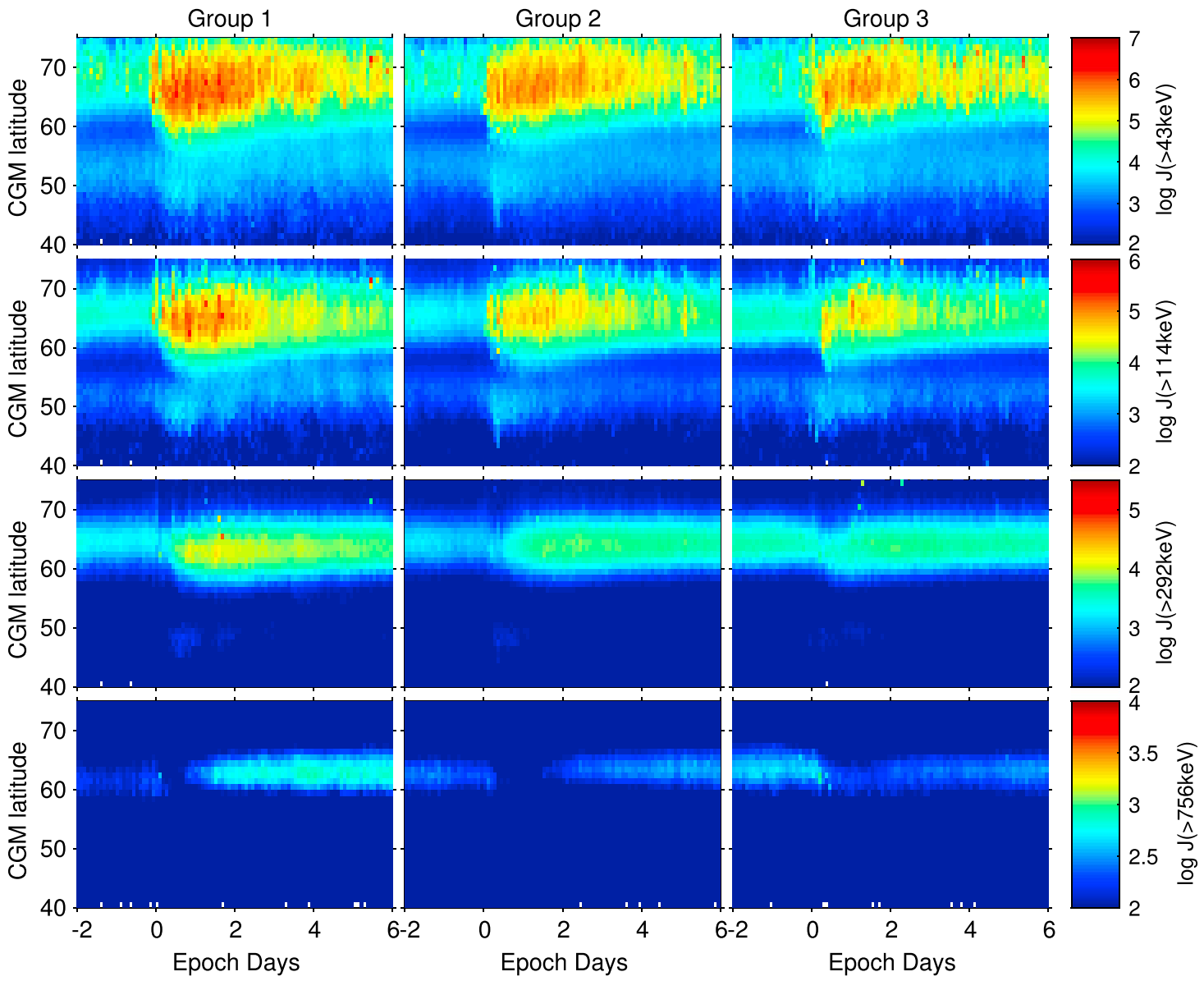

Figure 9. Superposed epoch analysis of 41 CIR/HSSWS storms from 2006 to 2010, divided into groups defined based on increase in P6 flux and E3 flux in the BLC precipitating fluxes. The mean flux between 55° and 70° CGM latitude and all MLT sectors of the two first days in the epoch is compared to the two last days in the epoch. The BLC fluxes are plotted in logarithmic color scale (in units of integral flux [cm^{-2} s^{-1} sr^{-1}]), and the data shown here are the mean over all MLT sectors. (top to bottom) E1, E2, E3, and P6 flux are shown. (left column) Events that have an increased flux in the P6 channel (group 1). (middle column) Events that have increased flux in the E3 channel but not the P6 channel are shown (group 2). (right column) Events that do not display increased fluxes in E3 or P6 (group 3). Note that the range of the colorbar is different for the four channels.

(in fact, they are so similar that it can be hard to see group 2 on the figure, because it is overplotted by group 3). Focusing on only the solar wind velocity after zero epoch, one would not tell groups 1 and 2 apart. Group 3 does not reach a maximum speed quite as high and also decreases faster after the maximum. The plateau of maximum speed is sustained for approximately 3 days in groups 1 and 2, but only little over 1.5 days in group 3.

The superposed epoch analysis of the BLC flux (mean over all MLT sectors) divided into groups is plotted in Figure 9, the trapped fluxes in Figure 10. Also for these plots, the standard deviation was found to be at least 1 order of magnitude smaller than the mean (not shown).

Group 1 events are characterized by the largest poststorm fluxes in all channels, both trapped and BLC flux. E3 trapped (BLC) flux increase by a factor of 11 (5), and for P6 by a factor of 7 (3). Group 2 events have the smallest prestorm E1 and E2 fluxes, both trapped and BLC flux. Group 3 events have the highest prestorm E3 and P6 fluxes, both trapped and BLC flux. In group 3 the total level of P6 flux decrease poststorm compared to prestorm.

4.1. The Energy Input From the Solar Wind to the Magnetosphere

Relating the findings from the superposed epoch analysis of fluxes to the superposed epoch analysis of solar wind measurements and geomagnetic indices, we investigate the relationship between fluxes and solar wind energy input to the magnetosphere closer. The simplest form of energy coupling function from the solar wind to the magnetosphere is the electric field [e.g., *Burton et al.*, 1975]. Interpreting the integrated electric field as a proxy for energy input, this suggests that group 1 consists of storms with a larger energy transfer.

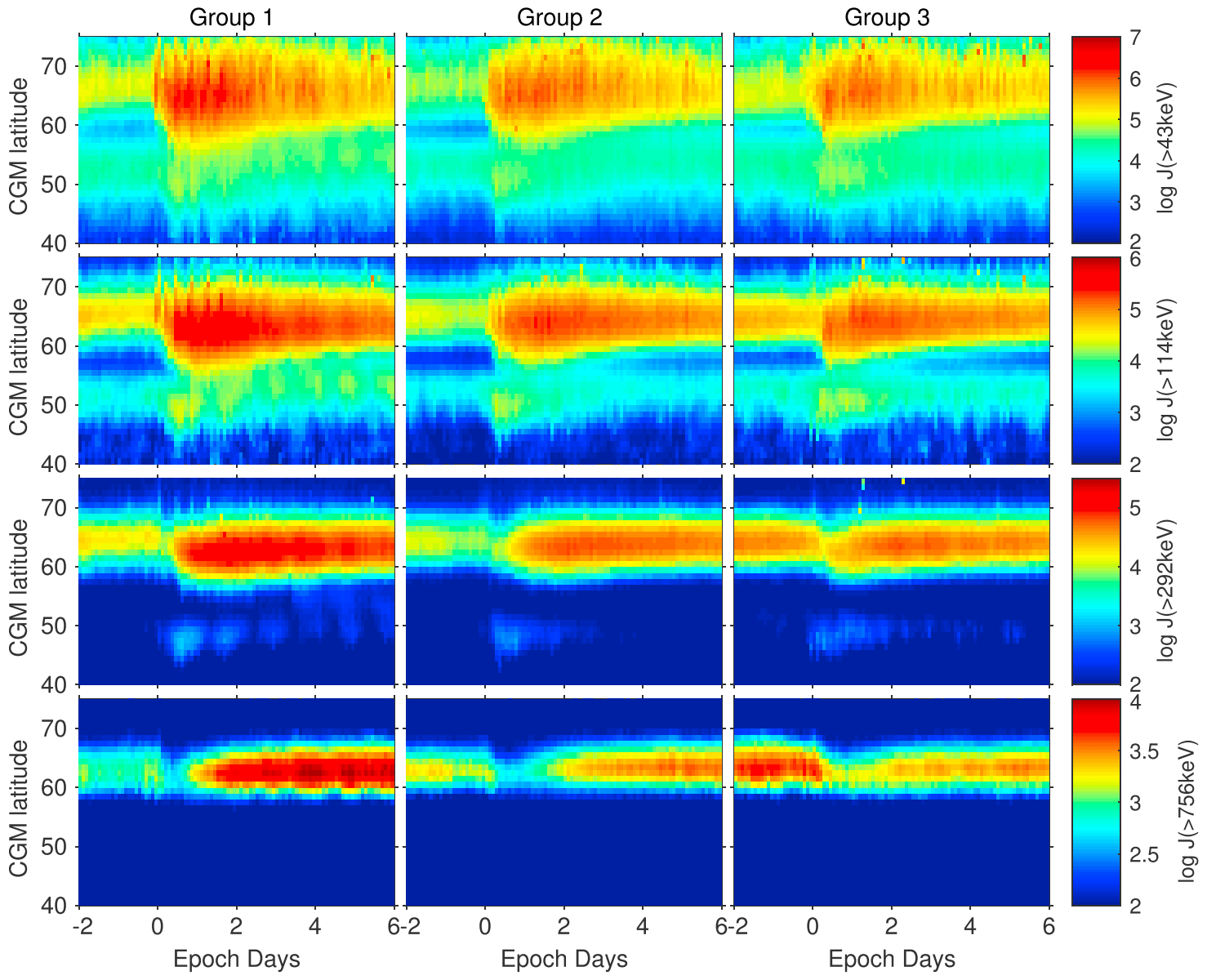

Figure 10. The same as in Figure 9 but here we plot 90° fluxes for the same groups. The range of the colorbar is identical to the BLC fluxes within each channel (and in units of integral flux [cm^{-2} s^{-1} sr^{-1}]). Groups are defined based on the BLC fluxes, see the text for a detailed description.

To investigate this closer, we instead calculate the energy input using the *Akasofu* [1981] epsilon parameter, given in SI units by *Koskinen* [2002]:

$$\varepsilon = \frac{4\pi}{\mu_0} VB^2 \sin^4\left(\frac{\theta}{2}\right) l_0^2 \tag{3}$$

where $\frac{4\pi}{\mu_0} = 10^7$, V is the solar wind velocity, B is the total solar wind magnetic field, θ is the clock angle (angle between the IMF vector and the Z axis, projected into the GSM Y-Z plane, $\tan\theta = \frac{B_y}{B_z}$), and $l_0 = 7R_E$. ε have the units of Watts. The mean ε for the three groups is also plotted in Figure 8.

If we integrate the epsilon parameter from zero epoch until the end of epoch for each group, we get 3.3×10^{18} J for group 1, 2.1×10^{18} J for group 2, and 2.2×10^{18} J for group 3. It is clear that the energy input is larger for group 1 after zero epoch. It does not, however, separate group 2 from group 3. When we study the fluxes in E3 of groups 2 and 3 more closely (Figures 9 and 10), we see that it is the prestorm level that separates these groups. When considering the poststorm flux in E3, there is little difference between the two groups.

To investigate the relationship between the precipitating fluxes and energy input more closely, we calculate the daily mean BLC flux over all MLT and CGM latitudes 55°–70° starting from zero epoch. From the daily means we subtract the mean BLC flux from −2 days to zero epoch. This leaves us with a daily net change in flux compared to the prestorm flux. We compare the daily change in flux with the integrated ε from zero epoch to, and including, the day in question.

For the E3 fluxes, we find the highest correlation on the third day after zero epoch. The results are shown in Figure 11 (left). In this figure, each storm is color coded according to which group it belongs to. The mean energy input for each group is plotted as dashed, vertical lines. The mean energy input for group 1 is a factor of 1.65 larger than for group 2 on days 3 and 4, and a factor of 1.82 larger than group 3. For the P6 fluxes,

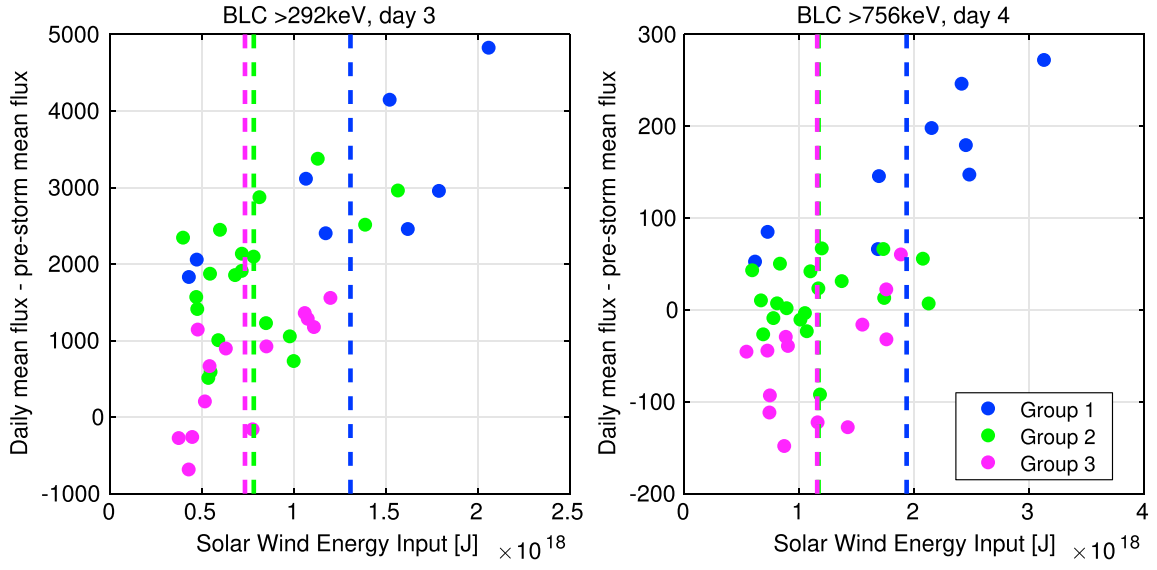

Figure 11. Prestorm flux calculated as mean over epoch hours −48 to 0, CGM latitude 55° – 70°, and all MLT. Daily mean BLC flux (starting with day 1 from zero epoch) is calculated over the same geomagnetic coordinates. We subtract prestorm flux from daily mean flux and plot versus the integrated ε parameter. The best correlation for E3 (P6) daily mean BLC flux is found on day 3 (4) versus energy input in Joules (integrated ε from zero epoch up to, and including, day 3 (4)). Correlation coefficient irrespective of group: E3, $r = 0.70$ and P6, $r = 0.68$. The mean energy input for each group is plotted as dashed vertical lines in the same color as the dots ((right) the green vertical dashed line is overplotted by the magenta line).

we find the best correlation on day 4. The results are shown in Figure 11 (right). The mean energy input for group 1 is a factor of 1.7 larger than for group 2, which is the same as found for E3 on the third day. The mean of group 1 is a factor of 1.8 larger than group 3 in P6 and 1.7 in E3.

There seems to be a limit of about 2.1×10^{18} J in the course of 4 days which has to be exceeded before electrons are accelerated to energies measured by the P6 channel and scattered into the loss cone. After this, the flux added to the loss cone (change from previous flux level) increases linearly. Below this limit, the change in flux appears more or less random for the P6 flux.

Disregarding the group the events belong to and correlating all 41 data points on the third (fourth) day, we find a correlation coefficient of 0.70 (0.68) for the E3 (P6) fluxes with the integrated ε. Looking only at group 1, the correlation coefficient is 0.72 (0.86). However, keep in mind that this is based on only nine events. A significant correlation of 0.75 is also found for group 3, E3 channel. The P6 fluxes show no significant correlation (to the 5% level) for group 2 and group 3.

4.2. The Dependence of the Precipitating Fluxes on the Radiation Belt Fluxes

The relationships between the ratio of poststorm to prestorm fluxes in the BLC and the 90° detector fluxes are shown for E3 and P6 in Figure 12. There are strong relationships between the trapped and BLC flux

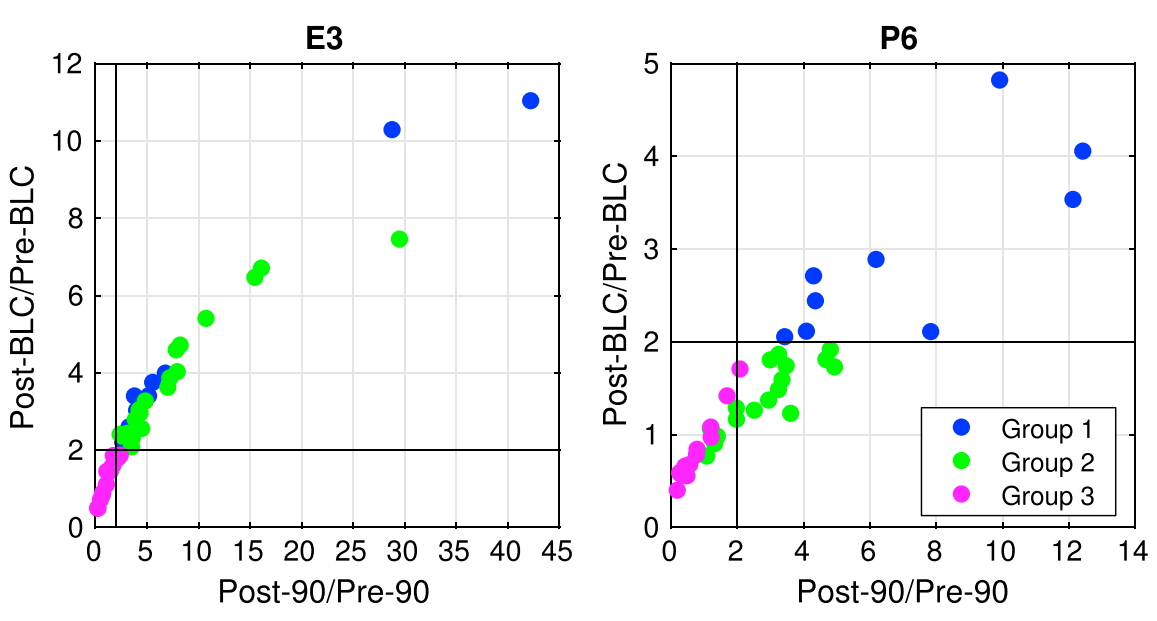

Figure 12. The ratios of postfluxes to prefluxes in BLC and 90° fluxes are scattered for all 41 storms ((left) E3, > 292 keV; (right) P6, > 756 keV). The color indicates which group the event belongs to, as defined based on the increase seen in BLC flux (see text for full description). Some of the blue dots are overplotted by green dots in Figure12 (left) (E3).

ratios both for the E3 and P6 fluxes; however, the relationships are not linear but better fit a power law of the form

$$y = ax^b \tag{4}$$

where y is the ratio post-BLC/pre-BLC flux, x is the ratio post-90/pre-90 flux, and the constants $a = 1.2$ (0.8) and $b = 0.6$ (0.6) for E3 (P6).

This implies that defining flux increase or decrease based on BLC or trapped fluxes will give different event selection into the groups. In this study we used the P6 BLC flux ratio (poststorm flux to prestorm flux) > 2 to define group 1 (blue circles). In Figure 12 (right), we see that all points above the horizontal line at BLC ratio $= 2$ are colored blue. Using the vertical line (ratio of trapped fluxes $= 2$) would produce a different set of storms belonging to group 1. The same is true for group 2, which is defined in the same way using the E3 fluxes (and subtracting the storms already sorted into group 1). This would also alter the superposed epoch analysis of solar wind parameters and geomagnetic indices, removing the characteristics of group 1 that were shown in Figure 8. This illustrates the added value and importance of studying precipitation from the radiation belts in itself, especially when considering the atmospheric effects. Using the BLC flux we get a new perspective on the processes important for the loss, and there exist a nonlinear dependence between the precipitation and the growth in the radiation belt for the CIR storms.

5. Discussion

The main focus of this work is to study weak to moderate geomagnetic disturbances caused by CIRs and to determine if they lead to precipitation of high-energy electrons from the radiation belts. The radiation belt is known to be highly dynamic during geomagnetic storms, and the competition between acceleration and loss processes determines the final response of the electron population. To have increased precipitation from the radiation belts in the recovery phase the total population has to increase, as confirmed by Figure 12. The relationship between geomagnetic storms and energization and acceleration of electrons is not fully understood [*Kessel*, 2016], and the response of the electron population to a storm does not necessarily scale with the size of the storm [*Anderson et al.*, 2015].

Higher-solar wind velocity has been noted by many to play a significant role in flux enhancements, but the relationship is not one-to-one [*Asikainen and Ruopsa*, 2016; *Kilpua et al.*, 2015; *Reeves et al.*, 2011]. As shown in Figure 8, we find a higher solar wind velocity sustained for a longer period in the groups of storms with enhanced precipitation of $> \sim 750$ keV (P6) and $> \sim 300$ keV (E3) (groups 1 and 2) compared to the group where flux increase is limited below a factor of 2 (group 3). As illustrated in the envelope of the solar wind B_Z component (Figure 2), magnetic field fluctuations are associated with CIR storms. This will cause intermittent intervals of enhanced magnetospheric convection and substorm activity [*Meredith et al.*, 2011] and subsequently acceleration and pitch angle scattering by associated wave activity.

The storms that caused increased precipitation of $> \sim 750$ keV electrons (group 1) showed a stronger mean signature in the *Dst*, *Dst**, *ap*, *AE*, *AU*, and *AL* indices (see Figure 8). The clearest parameter for separating the storms that caused the highest increase in $> \sim 750$ keV precipitation was an energy input $> 2.1 \times 10^{18}$ J over 4 days after zero epoch, as estimated by the integrated ε parameter. We also observed that the group of events with decreased or unchanged fluxes of $> \sim 300$ keV and $> \sim 750$ keV fluxes (group 3) has the highest average prestorm flux of the three groups (see Figure 9). In this group, it seems that a significant prestorm flux in the radiation belts are effectively lost when the storm onsets. However, the weak solar wind energy input later in the storm is not strong enough to fill the radiation belts and cause significant precipitation. Since the prestorm flux in these storms is higher compared to the two other groups, a strong solar wind driver would be needed to cause the flux to build up to the same or higher levels as before the storm started.

The energy input could not separate the storms in group 2 and group 3. In the solar wind parameters, groups 1 and 2 are mainly separated by group 1 having a more negative B_Z, which indicates a stronger energy transfer from the solar wind to the magnetosphere in the case of $> \sim 750$ keV precipitating fluxes. This was confirmed by the integrated ε parameter, showing a larger estimated energy input for group 1. This might be applied to improve the current energetic electron parametrizations which are usually based solely on geomagnetic indices. In particular, recent studies/review papers highlight the importance of a more accurate parametrization of energetic electron precipitation in order to correctly simulate the polar winter stratosphere-mesosphere region [e.g., *Rozanov et al.*, 2012; *Sinnhuber et al.*, 2012; *Randall et al.*, 2015].

The geomagnetic indices have strong limitations in this context. While the lower energy part of the electron precipitation spectrum is known to be closely correlated with geomagnetic indices [e.g., *Hendrickx et al.*, 2015], the higher electron energies are more ambiguous [*Turunen et al.*, 2009].

In summary, our findings suggest the solar wind speed and the electric field to be possible candidates for a parametrization of EEP. Elevated solar wind velocity for 3 days increases the likelihood of $> \sim 300$ keV precipitation, while the addition of a more negative B_Z increases the likelihood of $> \sim 750$ keV precipitation.

Additionally, a parametrization should also consider the local time variations and the time evolution of the events. The superposed epoch analysis of all 41 events divided into MLT sectors (Figures 3 and 4) showed that the trapped and BLC fluxes behaved in much the same manner, but with the trapped fluxes having larger intensities in all energy channels. Expected dropouts were seen in the $> \sim 300$ keV and $> \sim 750$ keV fluxes following main phase of the storm. Increasing delay in flux buildup with energy was also found. Both the trapped and the BLC fluxes decreased during main phase, implying that the disappearing flux was not mainly precipitated but lost to the magnetopause or influenced by adiabatic effects. These findings are in accordance with previous studies [*Reeves et al.*, 2003; *Millan and Thorne*, 2007; *Meredith et al.*, 2011; *Anderson et al.*, 2015]. As shown in Figure 8, the magnetopause (modeled as by *Shue et al.* [1998]) only moves into 8 R_E during the pressure enhancement associated with the CIR. Therefore, if magnetopause shadowing plays a role in the flux decrease from the trapped population, there needs to be significant outward radial transport. Electrons are known to move radially outward during the main phase to conserve their third invariant. *Turner et al.* [2012] point out that both enhanced dawn-dusk electric fields and diamagnetic effects from a partial ring current during the storm's main phase can result in violation of the third invariant and rapid outward radial transport, resulting in losses to the magnetopause in only a few hours. Also, a phase space density (PSD) that is decreasing with respect to increasing radial distance can result in outward radial diffusion as diffusion always acts to transport particles in the opposite direction to the PSD gradient. Finally, ultralow-frequency (ULF) waves can violate the third adiabatic invariant and allow for electron radial diffusion. Exemplified by a CIR event with *Dst* minimum > -50 nT, *Turner et al.* [2012] confirm that this mechanisms can indeed deplete the outer radiation belt above $L \sim 4R_E$ in only a few hours.

Using the trapped fluxes to define the three groups of events would provide different superposed epoch analyses, as opposed to using the BLC fluxes. This was shown in Figure 12. There is a strong relationship between the enhancement a storm produces in trapped and precipitated fluxes, but it is not a one-to-one, linear relationship. This may be important to keep in mind when atmospheric EEP effects are studied in relation to the radiation belt dynamics.

6. Conclusions

We have presented trapped and precipitating electron fluxes for 41 small to moderate storms associated with CIRs. We performed a superposed epoch analysis of the events divided into groups according to whether the storm increased precipitation of $> \sim 300$ keV or $> \sim 750$ keV electrons, when the 2 days before zero epoch were compared with the two last days in the epoch interval, over all MLTs and CGM latitude 55–70°. Nine storms that had post-P6 flux > 2×pre-P6 flux were sorted into group 1. From the remaining storms, 19 had post-E3 flux > 2×pre-E3flux and were sorted into group 2. The last 13 storms, where the fluxes of $> \sim 300$ keV and $> \sim 750$ keV were limited below an increase of a factor 2, were sorted into group 3.

A superposed epoch analysis of solar wind parameters divided into the three groups showed that the solar wind electric field was larger for group 1, as a result of a more negative B_Z component. We showed that the energy input from the solar wind to the magnetosphere was larger for group 1 compared to the two other groups. Together with the longer duration of enhanced solar wind velocity, the solar wind electric field stand out as possible parameters to predict whether a storm will cause enhanced precipitation with relativistic energy in the recovery phase. To accelerate and precipitate $> \sim 300$ keV electrons, elevated solar wind velocity over longer periods appears to be vital. We also illustrate the importance of an MLT consideration. For example, we find a localized loss to the atmosphere in the main phase in the MLT 18–22 sector at CGM latitudes around 60°.

Appendix A: Optimized Electron Energy Limits and Associated Geometric Factors

The nominal electron energy limits for the MEPED electron telescope were given as >30, >100, and >300 keV [*Evans and Greer*, 2000]. *Yando et al.* [2011] performed a Monte Carlo simulation of the response functions

Table A1. The Optimized Integral Energy Limit for Channels E1, E2, E3, and P6 and the Associated Geometric Factors

	E1	E2	E3	P6
Integral energy limit (keV)	43	114	292	756
Geometric factor[a]	1.01×10^{-2}	1.12×10^{-2}	8.08×10^{-3}	7.39×10^{-3}
Maximum positive deviation[b]	26	7	7	30
Maximum negative deviation[b]	20	6	11	17

[a]Given in units of cm^{-2} sr.
[b]Given in percent (%).

using the Geant4 code. The simulation reveals a fairly slant response function near the lower energy limit, in particular for the first electron energy channel. They found the effective range for E1 to be 50 keV. Effective range was defined as the energy limit which corresponds to a geometric factor half of the total instrument geometric value [*Yando et al.*, 2011, Table 3]. When in operation the true energy limits and the corresponding geometric factors will, however, depend on the incoming electron energy spectrum. Hence, *Green* [2013] calculated new energy limits and associated geometric factors based on a range of exponential spectra and power law spectra, optimized by using the Bowtie method. In respect to the three electron channels the derived, optimized center energies are associated with fairly large uncertainties. We also note that there generally is a large distance between the energy limit giving the minimum spread in geometric factor for power law spectra and exponential spectra. Therefore, based on the response functions given by *Yando et al.* [2011], we revisit the electron energy limits of the electron detector, as well as the electron response in the P6 channel. We aim to determine an optimized effective integral energy limit for the MEPED electron measurements.

Similar to *Green* [2013] we assume both power law and exponential spectra to give a reasonable representation of the incoming electron energies:

$$n_i = \int_{E=0}^{2.5\ \mathrm{MeV}} \mathrm{G}_i(E) E^{-\gamma} \mathrm{d}E,\ i = 1, 2, 3 \tag{A1}$$

$$n_i = \int_{E=0}^{2.5\ \mathrm{MeV}} \mathrm{G}_i(E) E^{\frac{-E}{E_0}} \mathrm{d}E,\ i = 1, 2, 3 \tag{A2}$$

where n_i is the normalized count rate for the three electron channels E1, E2, and E3. For practical reasons we have put an upper limit on the different energy channels. This limit is so high that it will not have a large effect on the flux of the integral spectrum for realistic spectral shapes. The geometric factors $\mathrm{G}_i(E)$ are taken from Table B4 in the supplemented with readings from Figure 5c in *Yando et al.* [2011] to obtain better energy resolution of the geometric factors near the lower energy thresholds of the three energy channels.

A similar procedure is used to calculate the count rate of electrons in the P6 channel, when P5 $\ll$ P6. Here we assume only a power spectrum:

$$n_{P6} = \int_{E=0}^{7\ \mathrm{MeV}} \mathrm{G}_{P6}(E) E^{-\gamma} \mathrm{d}E \tag{A3}$$

The geometric factors $\mathrm{G}_{P6}(E)$ are taken from Table B2 and Figure 8 in *Yando et al.* [2011]. The ranges of γ and E_0 used in equations (A1)–(A3) are given in Table A2.

Table A2. The Range of γ and E_0 Included in Equations (A1)–(A3)

	γ		E_0 keV	
Channel	Range	Step Size	Range	Step Size
E1	0.25–4.5	0.25	10–300	10
E2	0.25–4.5	0.25	20–400	10
E3	0.25–4.5	0.25	40–900	20
P6	0.25–4.5	0.25		

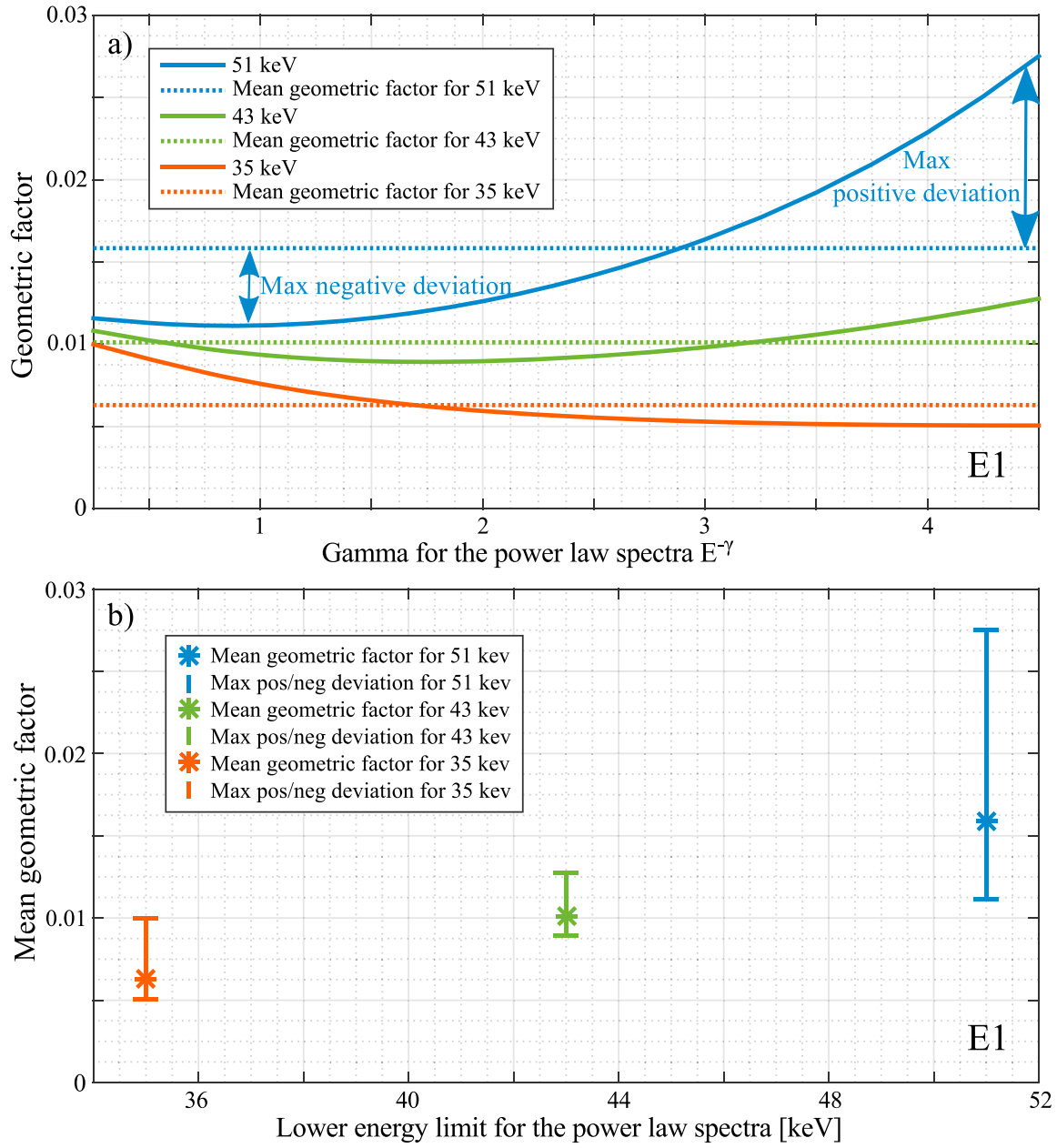

Figure A1. The Figure illustrates two steps of the method toward finding the optimized geometric factor for the E1 energy channel. (a) The geometric factor is plotted for different γ of the power law spectra. The three solid lines represent spectra where 35 keV (orange), 43 keV (green), or 51 keV (blue) are taken as the lower energy limit of the spectra. Each curve's mean geometric value is shown as dotted line. (b) The three mean geometric factors (shown as dotted lines in Figure A1a) are now plotted (as asterisk) versus the lower energy limit for the power law spectra. The vertical error bars in Figure A1b are the maximum positive and negative deviations shown as arrows in Figure A1a.

Afterward we calculate average geometric factors, $\bar{G}_i$ and $\bar{G}_{P6}$, for a dense set of γ and E_0 values for different values of the lower energy threshold, E_i and E_{P6}:

$$\bar{G}_i = \frac{n_i}{J_i(> E_i) - J_i(> 2.5\ \mathrm{MeV})} \tag{A4}$$

for E1, E2, and E3, and

$$\bar{G}_{P6} = \frac{n_{P6}}{J_{P6}(> E_{P6}) - J_{P6}(> 7\ \mathrm{MeV})} \tag{A5}$$

for P6.

Figure A1 illustrates different steps in the method of determining an optimized geometric factor, with the E1 channel used as an example. The Figure displays how the mean geometric factor is calculated for different values for the lower energy limit. To make the figure readable, we only show three examples here, 35 keV, 43 keV, and 51 keV. The example shown is for power law spectra, but the procedure is the same for the exponential spectra. In Figure A1a, the geometric factors are plotted as functions of γ for the three example lower energy limits. The mean of each curve is plotted as horizontal dotted lines in Figure A1a and asterisk in Figure A1b. The vertical error bars in Figure A1b are the maximum positive and negative deviations shown with arrows in Figure A1a.

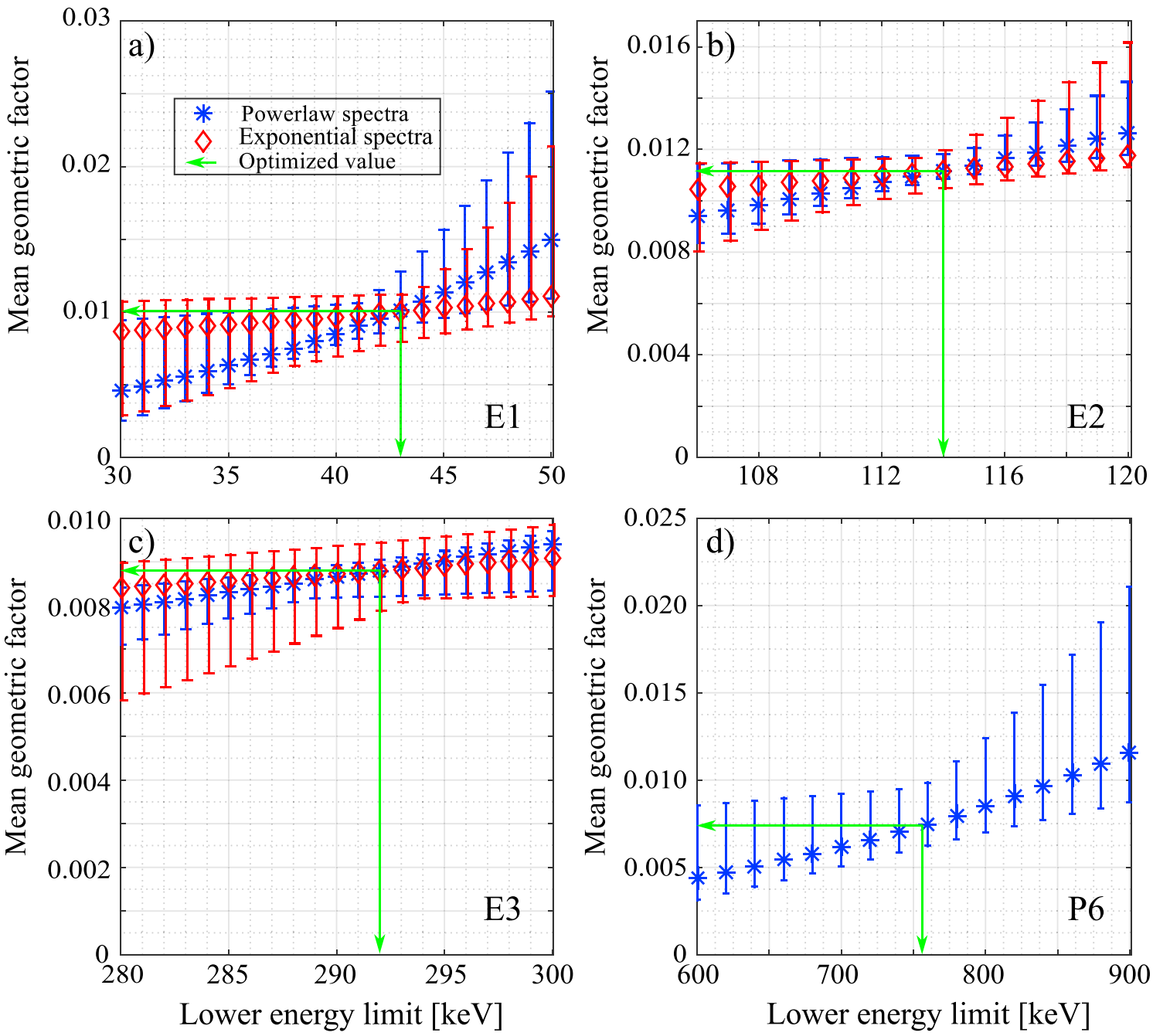

Figure A2. (a and b) The mean geometric factor as a function of the lower integral energy limit for channels E1 and E2 over the given range of γ and E_0 for power law (blue asterisk) and exponential spectra (red diamond), respectively. (c and d) The same for E3 and P6 (only power law). The associated maximum positive and negative percentage deviations are shown as vertical bars. The optimized integral energy limit and associated mean geometric factors from Table A1 are marked in all four panels as green vertical and horizontal lines.

Figure A2 show the derived results for (a) E1, (b) E2, (c) E3, and (d) P6, with power law spectra given in blue and exponential spectra in red. The aforementioned positive and negative deviations are also shown in each panel, as error bars. The optimized lower energy limit and associated geometric factor will be somewhat different for the power law spectra and exponential spectra. For example, in Figure A2a, we find, focusing on the power law spectra, that 41 keV and a geometric factor of 0.9×10^{-2} (cm^{-2} sr) gives the minimum deviation for the geometric factor over the range of γ values. For the exponential spectra, the energy and associated geometric factor is 43 keV and 1.01×10^{-2} (cm^{-2} sr). The optimized energy limit giving minimum deviation for all γ and E_0 is the energy of 43 keV and 1.01×10^{-2} (cm^{-2} sr). The optimized energy limits and associated geometric factor for E1, E2, E3, and P6 are given in Table A1.

In contrast to *Green* [2013] we find the optimized energy limits for power law and exponential spectra to be only a few keV apart. For example, for E2 the optimized energy for the power law spectra and exponential spectra is 113 and 115 keV, respectively. According to Figure 3-3 in *Green* [2013] the optimized energies are $\sim$ 122 and 160 keV. In general, we get a smaller maximum deviation for the geometric factor compared to *Green* [2013]. We base the range of γ and E_0 on the flux measurements from a 10 day period, 17–27 August 2005. It includes both low and high geomagnetic activity (*Kp* range: 0–9).

Appendix B: List of Storms Used in the Study

A list of storms used in this study is presented in Table B1.

Table B1. Date and Time of Zero Epoch of Identified Storms

Storm nr	Date	Time (UT)
1	18 May 2006	05:55
2	6 Jun 2006	10:35
3	14 Jun 2006	20:40
4	4 Jul 2006	12:35
5	7 Aug 2006	02:50
6	24 Sep 2006	01:25
7	12 Oct 2006	12:30
8	27 Oct 2006	22:35
9	9 Nov 2006	18:25
10	29 Jan 2007	06:20
11	27 Feb 2007	07:25
12	1 Apr 2007	00:05
13	22 May 2007	14:55
14	17 Dec 2007	05:40
15	31 Jan 2008	14:50
16	10 Feb 2008	05:40
17	8 Mar 2008	12:50
18	26 Mar 2008	09:20
19	4 Apr 2008	16:15
20	23 Apr 2008	05:00
21	14 Jun 2008	17:15
22	11 Jul 2008	23:20
23	22 Jul 2008	08:45
24	9 Aug 2008	04:40
25	4 Sep 2008	00:45
26	2 Oct 2008	09:10
27	11 Oct 2008	07:45
28	28 Oct 2008	10:30
29	7 Nov 2008	14:00
30	15 Nov 2008	17:30
31	14 Feb 2009	04:30
32	12 Mar 2009	20:20
33	21 Mar 2009	04:30
34	8 Apr 2009	18:10
35	19 Aug 2009	11:15
36	20 Jan 2010	16:35
37	10 Mar 2010	11:55
38	2 May 2010	08:15
39	15 Jun 2010	08:30
40	23 Aug 2010	22:20
41	23 Oct 2010	03:30

Acknowledgments
This study was supported by the Research Council of Norway/CoE under contract 223252/F50. The authors thank the NOAA's National Geophysical Data Center (NGDS) for providing NOAA data. The OMNI data were obtained from the GSFC/SPDF OMNIWeb interface at http://omniweb.gsfc.nasa.gov. The processed data used in this study are available upon request.

References

Akasofu, S.-I. (1981), Energy coupling between the solar wind and the magnetosphere, *Space Sci. Rev.*, *28*(1963), 121–190.

Anderson, B. R., R. M. Millan, G. D. Reeves, and R. H. W. Friedel (2015), Acceleration and loss of relativistic electrons during small geomagnetic storms, *Geophys. Res. Lett.*, *42*, 10,113–10,119, doi:10.1002/2015GL066376.

Andersson, M. E., P. T. Verronen, S. Wang, C. J. Rodger, M. A. Clilverd, and B. R. Carson (2012), Precipitating radiation belt electrons and enhancements of mesospheric hydroxyl during 2004–2009, *J. Geophys. Res.*, *117*, D09304, doi:10.1029/2011JD017246.

Andersson, M. E., P. T. Verronen, C. J. Rodger, M. A. Clilverd, and S. Wang (2014a), Longitudinal hotspots in the mesospheric OH variations due to energetic electron precipitation, *Atmos. Chem. Phys.*, *14*(2), 1095–1105, doi:10.5194/acp-14-1095-2014.

Andersson, M. E., P. T. Verronen, C. J. Rodger, M. A. Clilverd, and A. Seppälä (2014b), Missing driver in the Sun-Earth connection from energetic electron precipitation impacts mesospheric ozone, *Nat. Commun.*, *5*, 5197, doi:10.1038/ncomms6197.

Asikainen, T., and M. Ruopsa (2016), Solar wind drivers of energetic electron precipitation, *J. Geophys. Res. Space Physics*, *121*, 1–50, doi:10.1002/2015JA022215.

Blum, L., X. Li, and M. Denton (2015), Rapid MeV electron precipitation as observed by SAMPEX/HILT during high-speed stream-driven storms, *J. Geophys. Res. Space Physics*, *120*, 3783–3794, doi:10.1002/2014JA020633.

Borovsky, J. E., and M. H. Denton (2006), Differences between CME-driven storms and CIR-driven storms, *J. Geophys. Res.*, *111*, A07S08, doi:10.1029/2005JA011447.

Burton, R. K., R. L. McPherron, and C. T. Russell (1975), An empirical relationship between interplanetary conditions and *Dst*, *J. Geophys. Res.*, *80*(31), 4204–4214.

Clilverd, M. A., C. J. Rodger, T. Moffat-Griffin, E. Spanswick, P. Breen, F. W. Menk, R. S. Grew, K. Hayashi, and I. R. Mann (2010), Energetic outer radiation belt electron precipitation during recurrent solar activity, *J. Geophys. Res.*, *115*, 1–15, doi:10.1029/2009JA015204.

Daae, M., P. Espy, H. Nesse Tyssøy, D. Newnham, J. Stadsnes, and F. Søraas (2012), The effect of energetic electron precipitation on middle mesospheric night-time ozone during and after a moderate geomagnetic storm, *Geophys. Res. Lett.*, *39*, L21811, doi:10.1029/2012GL053787.

Evans, D. S., and M. S. Greer (2000), *Polar Orbiting Environmental Satellite Space Environment Monitor—2 Instrument Descriptions and Archive Data Documentation*, NOAA Technical Memorandum OAR SEC 93, version 1.4, Natl. Atmos. and Oceanic Admin., Space Environ. Cent., Boulder, Colo.

Frank, L. A., J. A. Van Allen, and J. D. Craven (1964), Large diurnal variations of geomagnetically trapped and of precipitated electrons observed at low altitudes, *J. Geophys. Res.*, *69*(15), 3155–3167, doi:10.1029/JZ069i015p03155.

Friedel, R. H. W., E. G. D. Reeves, and T. Obara (2002), Relativistic electron dynamics in the inner magnetosphere—A review, *J. Atmos. Sol. Terr. Phys.*, *64*(2), 265–282, doi:10.1016/S1364-6826(01)00088-8.

Gonzalez, W. D., J. A. Joselyn, Y. Kamide, H. W. Kroehl, G. Rostoker, B. T. Tsurutani, and V. M. Vasyliunas (1994), What is a geomagnetic storm?, *J. Geophys. Res.*, *99*(A4), 5771, doi:10.1029/93JA02867.

Green, J. (2013), MEPED telescope data processing theoretical basis document version 1.0, NOAA Technical Memorandum, version 1.0. [Available at http://www.ngdc.noaa.gov/stp/satellite/poes/documentation.html.]

Hendrickx, K., L. Megner, J. Gumbel, D. E. Siskind, Y. J. Orsolini, H. Nesse Tyssøy, and M. Hevig (2015), Observation of 27 day solar cycles in the production and mesospheric descent of EPP-produced NO, *J. Geophys. Res. Space Physics*, *120*, 8978–8988, doi:10.1002/2015JA021441.

Horne, R. B., M. M. Lam, and J. C. Green (2009), Energetic electron precipitation from the outer radiation belt during geomagnetic storms, *Geophys. Res. Lett.*, *36*, L19104, doi:10.1029/2009GL040236.

Kavanagh, A. J., F. Honary, E. F. Donovan, T. Ulich, and M. H. Denton (2012), Key features of >30 keV electron precipitation during high speed solar wind streams: A superposed epoch analysis, *J. Geophys. Res.*, *117*, 1–13, doi:10.1029/2011JA017320.

Kennel, C. F., and H. E. Petschek (1966), Limit on stably trapped particle fluxes, *J. Geophys. Res.*, *71*(1), 1–28.

Kessel, M. (2016), Things we don't yet understand about solar driving of the radiation belts, *J. Geophys. Res. Space Physics*, *121*(6), 5549–5552, doi:10.1002/2016JA022472.

Kilpua, E., H. Hietala, D. L. Turner, H. E. J. Koskinen, T. I. Pulkkinen, J. V. Rodriguez, E. G. D. Reeves, S. G. Claudepierre, and H. E. Spence (2015), Unraveling the drivers of the storm-time radiation belt response, *Geophys. Res. Lett.*, *42*, 3076–3084, doi:10.1002/2015GL063542.

Koskinen, H. E. J. (2002), Magnetospheric energy budget and the epsilon parameter, *J. Geophys. Res.*, *107*(A11), 1415, doi:10.1029/2002JA009283.

Lam, M. M., R. Horne, N. P. Meredith, S. A. Glauert, T. Moffat-Griffin, and J. C. Green (2010), Origin of energetic electron precipitation >30 keV into the atmosphere, *J. Geophys. Res.*, *115*, A00F08, doi:10.1029/2009JA014619.

Meredith, N. P., R. B. Horne, M. M. Lam, M. H. Denton, J. E. Borovsky, and J. C. Green (2011), Energetic electron precipitation during high-speed solar wind stream driven storms, *J. Geophys. Res.*, *116*, 1–16, doi:10.1029/2010JA016293.

Millan, R. M., and D. N. Baker (2012), Acceleration of particles to high energies in Earth's radiation belts, *Space Sci. Rev.*, *173*(1–4), 103–131, doi:10.1007/s11214-012-9941-x.

Millan, R. M., and R. M. Thorne (2007), Review of radiation belt relativistic electron losses, *J. Atmos. Sol. Terr. Phys.*, *69*(3), 362–377, doi:10.1016/j.jastp.2006.06.019.

Nesse Tyssøy, H., M. I. Sandanger, L.-K. G. Ødegaard, J. Stadsnes, A. Aasnes, and A. E. Zawedde (2016), Energetic electron precipitation into the middle atmosphere—Constructing the loss cone fluxes from MEPED POES, *121*, 5693–5707, doi:10.1002/2016JA022752.

Ødegaard, L.-K. G., H. Nesse Tyssøy, M. I. Jakobsen, J. Stadsnes, and F. Søraas (2016), Space weather impact on the degradation of NOAA POES MEPED proton detectors, *J. Space Weather Space Clim.*, *6*(A26), doi:10.1051/swsc/2016020.

Ødegaard, L.-K. G. (2016), Energetic particle precipitation into the middle atmosphere—Optimization and applications of the NOAA POES MEPED data, PhD. thesis, Univ. of Bergen, Bergen, Norway.

Randall, C. E., V. L. Harvey, L. A. Holt, D. R. Marsh, D. Kinnison, B. Funke, and P. F. Bernath (2015), Simulation of energetic particle precipitation effects during the 2003–2004 Arctic winter, *Geophys. Res. Lett.*, *120*, 5035–5048, doi:10.1002/2015JA021196.

Reeves, E. G. D., K. L. McAdams, R. H. W. Friedel, and T. P. O'Brien (2003), Acceleration and loss of relativistic electrons during geomagnetic storms, *Geophys. Res. Lett.*, *30*(10), 1529, doi:10.1029/2002GL016513.

Reeves, E. G. D., S. K. Morley, R. H. W. Friedel, M. G. Henderson, T. E. Cayton, G. Cunningham, J. B. Blake, R. a. Christensen, and D. Thomsen (2011), On the relationship between relativistic electron flux and solar wind velocity: Paulikas and Blake revisited, *J. Geophys. Res.*, *116*, A02213, doi:10.1029/2010JA015735.

Reeves, E. G. D., et al. (2013), Electron acceleration in the heart of the Van Allen radiation belts, *Science*, *341*.

Richardson, I. (2006), The formation of CIRs at stream-stream interfaces and resultant geomagnetic activity, in *Recurrent Magnetic Storms: Corotating Solar Wind Streams, Geophys. Monogr. Ser.*, vol. 167, pp. 45–58, AGU, Washington, D. C., doi:10.1029/167GM06.

Richardson, I. G., and H. V. Cane (2010), Near-Earth interplanetary coronal mass ejections during solar cycle 23 (1996–2009): Catalog and summary of properties, *Sol. Phys.*, *264*(1), 189–237, doi:10.1007/s11207-010-9568-6.

Rodger, C. J., M. A. Clilverd, J. C. Green, and M. M. Lam (2010a), Use of POES SEM-2 observations to examine radiation belt dynamics and energetic electron precipitation into the atmosphere, *J. Geophys. Res.*, *115*, A04202, doi:10.1029/2008JA014023.

Rodger, C. J., M. A. Clilverd, A. Seppälä, N. R. Thomson, R. J. Gamble, M. Parrot, J. A. Sauvaud, and T. Ulich (2010b), Radiation belt electron precipitation due to geomagnetic storms: Significance to middle atmosphere ozone chemistry, *J. Geophys. Res.*, *115*, 1–12, doi:10.1029/2010JA015599.

Rodger, C. J., B. R. Carson, S. A. Cummer, R. J. Gamble, M. A. Clilverd, J. C. Green, J. A. Sauvaud, M. Parrot, and J. J. Berthelier (2010c), Contrasting the efficiency of radiation belt losses caused by ducted and nonducted whistler-mode waves from ground-based transmitters, *J. Geophys. Res.*, *115*, 1–13, doi:10.1029/2010JA015880.

Rodger, C. J., A. J. Kavanagh, M. A. Clilverd, and S. R. Marple (2013), Comparison between POES energetic electron precipitation observations and riometer absorptions: Implications for determining true precipitation fluxes, *J. Geophys. Res. Space Physics*, *118*, 7810–7821, doi:10.1002/2013JA019439.

Rodger, C. J., A. T. Hendry, M. A. Clilverd, C. A. Kletzing, J. B. Brundell, and E. G. D. Reeves (2015), High-resolution in situ observations of electron precipitation-causing EMIC waves, *Geophys. Res. Lett.*, *42*, 9633–9641, doi:10.1002/2015GL066581.

Rozanov, E., M. Calisto, T. Egorova, T. Peter, and W. Schmutz (2012), Influence of the precipitating energetic particles on atmospheric chemistry and climate, *Surv. Geophys.*, *33*(3–4), 483–501, doi:10.1007/s10712-012-9192-0.

Sandanger, M. I., L.-K. G. Ødegaard, H. Nesse Tyssøy, J. Stadsnes, F. Søraas, K. Oksavik, and K. Aarsnes (2015), In-flight calibration of NOAA POES proton detectors—Derivation of the MEPED correction factors, *J. Geophys. Res. Space Physics*, *120*, 9578–9593, doi:10.1002/2015JA021388.

Seppälä, A., and M. A. Clilverd (2014), Energetic particle forcing of the Northern Hemisphere winter stratosphere: Comparison to solar irradiance forcing, *Front Phys.*, *2*, 1–6, doi:10.3389/fphy.2014.00025.

Seppälä, A., C. E. Randall, M. A. Clilverd, E. Rozanov, and C. J. Rodger (2009), Geomagnetic activity and polar surface air temperature variability, *J. Geophys. Res.*, *114*, 1–10, doi:10.1029/2008JA014029.

Seppälä, A., H. Lu, M. A. Clilverd, and C. J. Rodger (2013), Geomagnetic activity signatures in wintertime stratosphere wind, temperature, and wave response, *J. Geophys. Res. Atmos.*, *118*, 2169–2183, doi:10.1002/jgrd.50236.

Seppäla, A., M. A. Clilverd, M. J. Beharrell, C. J. Rodger, P. T. Verronen, M. E. Andersson, and D. Newnham (2015), Substorm-induced energetic electron precipitation: Impact on atmospheric chemistry, *Geophys. Res. Lett.*, *42*, 8172–8176, doi:10.1002/2015GL065523.

Shue, J. H., et al. (1998), Magnetopause location under extreme solar wind conditions, *J. Geophys. Res.*, *103*(A8), 1281–1334, doi:10.1029/98JA01103.

Sinnhuber, M., H. Nieder, and N. Wieters (2012), Energetic particle precipitation and the chemistry of the mesosphere/lower thermosphere, *Surv. Geophys.*, *33*(6), 1281–1334, doi:10.1007/s10712-012-9201-3.

Søraas, F., K. Aarsnes, K. Oksavik, M. I. Sandanger, D. S. Evans, and M. S. Greer (2004), Evidence for particle injection as the cause of *Dst* reduction during HILDCAA events, *J. Atmos. Sol. Terr. Phys.*, *66*(2), 177–186, doi:10.1016/j.jastp.2003.05.001.

Summers, D., N. Binbin, and N. P. Meredith (2007), Timescales for radiation belt electron acceleration and loss due to resonant wave-particle interactions: 2. Evaluation for VLF chorus, ELF hiss, and electromagnetic ion cyclotron waves, *J. Geophys. Res.*, *112*, 1–21, doi:10.1029/2006JA011993.

Theodoridis, G. C., and F. R. Paolini (1967), Pitch angle diffusion of relativistic outer belt electrons, *Ann. Geophys.*, *23*, 375–380.

Tsurutani, B. T., and G. S. Lakhina (1997), Some basic concepts of wave-particle interactions in collisionless plasmas, *Rev. Geophys.*, *35*(4), 491–502.

Tsurutani, B. T., et al. (2006a), Corotating solar wind streams and recurrent geomagnetic activity: A review, *J. Geophys. Res.*, *111*, A07S01, doi:10.1029/2005JA011273.

Tsurutani, B. T., R. L. McPherron, W. D. Gonzalez, G. Lu, N. Gopalswamy, and F. L. Guarnieri (2006b), Magnetic storms caused by corotating solar wind streams, in *Recurrent Magnetic Storms: Corotating Solar Wind Streams, Geophys. Monogr. Ser.*, vol. 167, edited by B. T. Tsurutani et al., pp. 1–17, AGU, Washington, D. C., doi:10.1029/167GM03.

Turner, D. L., Y. Shprits, M. Hartinger, and V. Angelopoulos (2012), Explaining sudden loss of outer radiation belt electrons during geomagnetic storms, *Nat. Phys.*, *8*, 202–212, doi:10.1038/nphys2185.

Turunen, E., P. T. Verronen, A. Seppälä, C. J. Rodger, M. A. Clilverd, J. Tamminen, C.-F. Enell, and T. Ulich (2009), Impact of different energies of precipitating particles on NO_X generation in the middle and upper atmosphere during geomagnetic storms, *J. Atmos. Sol. Terr. Phys.*, *71*(10–11), 1176–1189, doi:10.1016/j.jastp.2008.07.005.

Williams, D. J., and W. F. Palmer (1965), Distortions in the radiation cavity as measured by an 1100-kilometer polar orbiting satellite, *J. Geophys. Res.*, *70*(3), 557–567.

Yando, K. B., R. M. Millan, J. C. Green, and D. S. Evans (2011), A Monte Carlo simulation of the NOAA POES Medium Energy Proton and Electron Detector instrument, *J. Geophys. Res.*, *116*, A10231, doi:10.1029/2011JA016671.

Zawedde, A. E., H. N. Tyssøy, J. Stadsnes, L.-K. Ødegaard, M. I. Sandanger, P. J. Espy, and R. Hibbins (2016), The impact of energetic electron precipitation on mesospheric hydroxyl during a year of solar minimum, *J. Geophys. Res.*, *121*, 5914–5929, doi:10.1002/2016JA022371.

Erratum

In the originally published version of this article, two errors were detected. The units specified in footnote "a" of Table A1 have been corrected to read "cm^{-2} sr". Also, in the next to last paragraph of Appendix A, all instances of "$(cm^2\ s\ str)^{-1}$" have been corrected to read "$(cm^{-2}$ sr)." The current version may be considered the authoritative version of record.